


Master Project in Electrical and Electronic Engineering

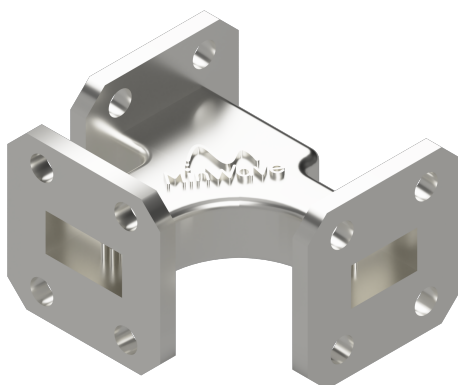
RF Measurements of Unconventional Miniaturised Filters and Diplexers

Robin Frédéric Bonny 
robin.bonny@alumni.epfl.ch

Supervised by:

Prof. Romain Fleury
LWE
romain.fleury@epfl.ch

Dr. Maliheh Khatibi
MinWave
m.khatibi@minwave.ch



Laboratory of Wave Engineering (LWE)
Section of Electrical and Electronic Engineering
École Polytechnique Fédérale de Lausanne

EPFL

Lausanne, Switzerland

Spring Semester 2023

23/06/2023

Contents

1	Acknowledgements	4
2	Introduction	5
3	Waveguides	6
3.1	Waveguide Theory	6
3.2	Waveguide Tapers	7
4	Network Analysis	10
4.1	Wave Parameters	10
4.2	Scattering Parameters	11
4.3	Alternative Expressions & Cascades	12
5	Error Models & Calibration	13
5.1	Error Models	13
5.2	Calibration Methods	14
5.3	Fixture Compensation	16
5.4	Further Remarks	16
6	Unterminating & De-Embedding	17
6.1	Relation to Error Models	18
6.2	Unterminating	18
6.3	De-Embedding	20
6.4	Port Augmentation	21
7	Measurements	24
7.1	Calibration Methods	24
7.2	Double-Ridged Waveguides	24
7.3	Diplexer	31
8	Discussion	38
8.1	Bisection Methods	38
8.2	Unterminating & De-Embedding Conclusions	38
8.3	Passivity	38
8.4	Port Augmentation	39
8.5	Characteristic Impedances	39
9	Conclusion	41
A	Definitions and Conventions	50
B	Measurement Results	52
C	Code Listings	59

1

Acknowledgements

I would like to express my sincere gratitude to the following individuals who have provided valuable support and assistance throughout the completion of this project:

Firstly, I would like to thank my supervisors, Romain Fleury and Maliheh Khatibi, for their support and for trusting me to define the direction of my research. I am also grateful to the employees of MinWave, especially Mostafa Khosrow, for his valuable input in various aspects and to Mehri Ziaee for validating my simulation results on multiple occasions.

I extend my thanks to all members of the Laboratory of Wave Engineering (LWE) and the Microwave and Antenna Group (MAG), with a special mention to Hannes Bartle, Erik Algarp, Ismael Vico Triviño, and Germán Ramírez Arroyave for their help in addressing theoretical and practical challenges related to waveguides and measurement techniques. I would like to acknowledge Miroslav Veljovic for introducing me to this project and Eva Mompert for her administrative support. I thank Tim Tuuva for generously allowing me to use his scripts for VNA data acquisition, significantly improving the efficiency of my measurement setup, as well as Ivan Tomic for his guidance and advice in the mechanical workshop.

I would like to express my appreciation to my good friend Martin Simik for his consistent motivation in collaborating on various projects related to RF and telecom engineering. On a more personal level, I am grateful to Valérie Luterbacher for her continued encouragement and reassurance, motivating me to overstep my own boundaries and embrace new challenges. Lastly, I would like to convey my deep appreciation to my parents for their support throughout my academic journey at EPFL over the last six years.

Introduction

This project aims to study and establish different measurement techniques to characterise the behaviour of waveguide devices, including filters and diplexers developed by MinWave¹, such as the diplexer shown on the title page. MinWave's core competency is an innovative design framework for at least ten times smaller and lighter micro/millimetre-wave waveguide devices and the fabrication of these components using additive manufacturing methods.

The complexity of the main measurement problems arises from distinct properties of the considered Devices Under Test (DUTs). These challenges have been solved independently in various prior works, but connecting these problems and verifying the underlying assumptions was crucial for this particular development. Including, but not limited to, the following aspects:

- **Multi-Port Networks**

Most similar analyses and measurements apply to two-port networks. A multi-port network, such as the three-port diplexer considered in this project, requires adequate termination of the additional ports and, therefore, a fusion of individual measurements to characterise the DUT entirely.

- **Non-Standard Flanges**

The studied diplexer features non-standard interfaces on its three ports, requiring the design and fabrication of well-characterised transitions and tapers to interface with the measurement setup.

- **Asymmetric Network**

In addition to the non-standard flanges, the considered diplexer employs flanges of different sizes for non-contiguous frequency channels, implying a difference in the propagating modes on different ports. Therefore, again, requiring properly designed transitions and tapers.

The central problem was subdivided into specific problems, which were evaluated and solved individually. Overall, the methods have been developed with potential extensions for millimetre wave devices with respect to satellite communications and 5G applications.

¹<https://www.minwave.ch/>

Waveguides

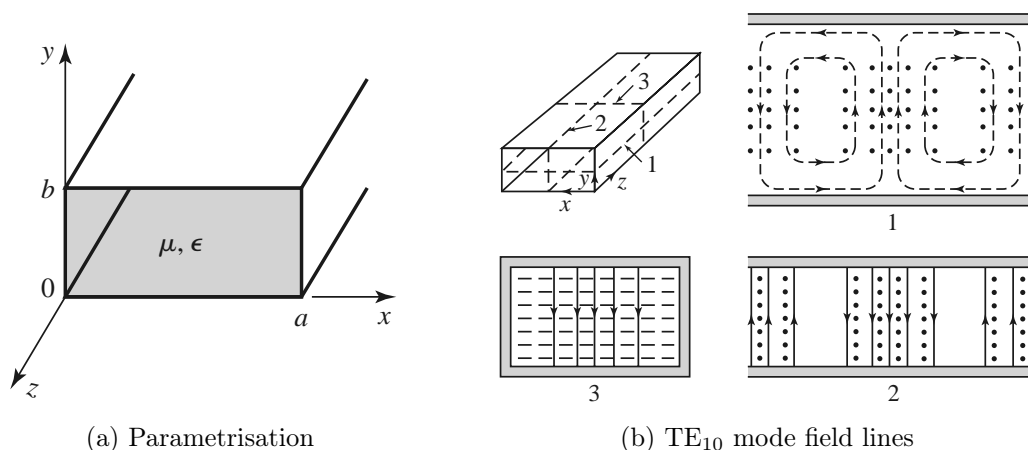


Figure 3.1: Rectangular waveguide illustrations, reproduced from [1, p. 131, 138]

3.1 Waveguide Theory

This chapter provides some excerpts on the theory and behaviour of waveguides, to an extent relevant for the development of this project, adapted from Pozar [1, p. 110-115].

3.1.1 General Considerations

The geometry of a rectangular waveguide, filled with a medium with properties μ and ε , with convention $a > b$, is shown in Figure 3.1a. For the waveguides used in this project, the frequency ranges of single-mode operation are considered; therefore, the subsequent theoretical developments focus uniquely on the fundamental mode (i.e. TE_{10}). In such a case, the longitudinal component of the electric field is equal to zero; the longitudinal magnetic field component is equal to the expression shown in Equation 3.1, and the remaining field components are shown in Equation 3.2. The field lines of the fundamental mode are shown in Figure 3.1b.

$$H_{z10} = A \cos\left(\frac{\pi x}{a}\right) e^{-j\beta z} \quad (3.1)$$

$$E_{x10} = 0 \quad (3.2a)$$

$$E_{y10} = -\frac{j\omega\mu a}{\pi} A \sin\left(\frac{\pi x}{a}\right) e^{-j\beta z} \quad (3.2b)$$

$$H_{x10} = \frac{j\beta a}{\pi} A \sin\left(\frac{\pi x}{a}\right) e^{-j\beta z} \quad (3.2c)$$

$$H_{y10} = 0 \quad (3.2d)$$

The value of the propagation constant is shown in Equation 3.3, based on the values of the wave number k and the cutoff wave number k_c . Furthermore, if a mode is propagating within the waveguide, the relation shown in Equation 3.4 holds.

$$\beta_{10} = \sqrt{k^2 - k_{c10}^2} = \sqrt{k^2 - \left(\frac{\pi}{a}\right)^2} \quad (3.3)$$

$$\omega\sqrt{\mu\varepsilon} = k > k_{c10} = \frac{\pi}{a} \quad (3.4)$$

3.1.2 Cutoff Frequency

The cutoff frequency of any given mode with modal indices m and n is computed using Equation 3.5. In the case of the fundamental mode, this expression reduces to a value only dependent on a and the propagating medium, as shown in Equation 3.6. A table of cutoff frequencies for various waveguide sizes, computed using Equation 3.5, can be found in Table A.2 within Appendix A. The single mode region of the waveguide is the frequency range in-between the cutoff of the fundamental mode and the cutoff of the first higher-order mode.

$$f_{c_{mn}} = \frac{1}{2\pi\sqrt{\mu\varepsilon}} \sqrt{\left(\frac{m\pi}{a}\right)^2 + \left(\frac{n\pi}{b}\right)^2} \quad (3.5)$$

$$f_{c_{10}} = \frac{1}{2a\sqrt{\mu\varepsilon}} \quad (3.6)$$

3.1.3 Waveguide Impedance

The TE wave impedance relates the amplitude of the orthogonal components of the electric and magnetic field as shown in Equation 3.7, which is frequency dependent. The expression shown in Equation 3.8 is obtained through simplification to the fundamental mode. The resulting parameter $\eta = \sqrt{\mu/\varepsilon}$ is the intrinsic impedance of the material filling the waveguide, becoming the impedance of free space Z_0 [2, p. 297] when approximating the interior to a vacuum. An alternative equivalent expression based on the cutoff frequency derived from Seeger [3, p. 53] is shown in Equation 3.9. Figure 3.2 shows the fundamental mode impedance of an arbitrary waveguide mode with a cutoff frequency of $f_c = 10$ GHz. Above cutoff, the waveguide impedance is purely real, asymptotically approaching the value of Z_0 with increasing frequency; below cutoff, the impedance is purely reactive (i.e. capacitive).

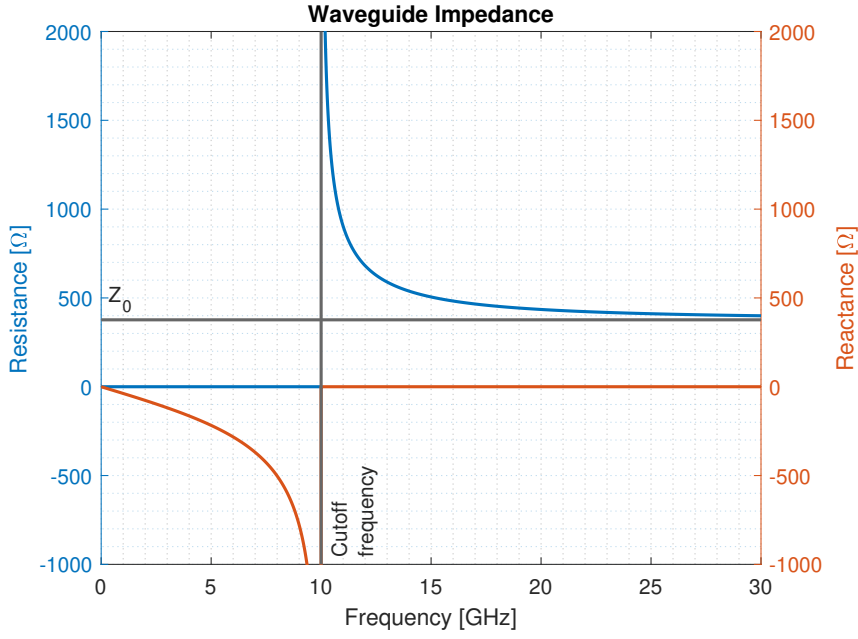
$$Z_{\text{TE}} = \frac{E_x}{H_y} = -\frac{E_y}{H_x} \quad (3.7)$$

$$Z_{\text{TE}10} = -\frac{E_{y10}}{H_{x10}} = \frac{-\frac{j\omega\mu a}{\pi} A \sin\left(\frac{\pi x}{a}\right) e^{-j\beta z}}{\frac{j\beta a}{\pi} A \sin\left(\frac{\pi x}{a}\right) e^{-j\beta z}} = \frac{\omega\mu}{\beta} = \frac{k\eta}{\beta} \quad (3.8)$$

$$Z_{\text{TE}} = \frac{Z_0}{\sqrt{1 - (f_c/f)^2}} \quad (3.9)$$

3.2 Waveguide Tapers

As mentioned in the introduction, the measurement setup requires the use of transitions from one waveguide cross-section to another. These components are hereafter referred to as *tapers*.

Figure 3.2: Waveguide fundamental mode impedance with $f_c = 10$ GHz

3.2.1 Linear Taper Profiles

Johnson lays out a synthesis method for the design of linear double tapers in rectangular waveguides [4]. In such a case, both dimensions a and b follow a linear profile between the two flanges. Parameters a_0 and b_0 denote the channel dimensions of the starting flange, a_1 and b_1 the channel dimensions of the ending flange, respectively. As all of the employed waveguides are air-filled at atmospheric pressure, the propagating velocity within the waveguide is assumed to be equal to the speed of light in a vacuum (i.e. $c = c_0$). The behaviour of the waveguides is obtained by first computing parameters K_0 , K_1 , and l , as shown in Equation 3.10. Subsequently, the absolute magnitude of the reflection coefficient is obtained using Equation 3.11. Using the well-known relation of Equation 3.12 [1, p. 58], the magnitude of the reflection coefficient is converted to the Voltage Standing Wave Ratio (VSWR). Listing C.1 demonstrates the corresponding MATLAB function implementation.

$$K_0 = \frac{\frac{b_1 - b_0}{b_0} - \frac{\frac{a_1 - a_0}{a_0}}{1 - \left(\frac{\lambda}{2a_0}\right)^2}}{\sqrt{1 - \left(\frac{\lambda}{2a_0}\right)^2}} \quad K_1 = \frac{\frac{b_1 - b_0}{b_1} - \frac{\frac{a_1 - a_0}{a_1}}{1 - \left(\frac{\lambda}{2a_1}\right)^2}}{\sqrt{1 - \left(\frac{\lambda}{2a_1}\right)^2}} \quad (3.10a)$$

$$l = \frac{1}{\lambda} \int_0^L \sqrt{1 - \left(\frac{\lambda}{2a}\right)^2} dx \quad (3.10b)$$

$$|\Gamma| = \frac{1}{L/\lambda} \sqrt{\frac{K_0^2 + K_1^2}{64\pi^2} - \frac{K_0 K_1}{32\pi^2} \cos(4\pi l)} \quad (3.11)$$

$$\text{VSWR} = \frac{1 + |\Gamma|}{1 - |\Gamma|} \quad (3.12)$$

This procedure is used to optimise the length L to minimise the VSWR of the tapers, ensuring that a maximum amount of power is injected into the subsequent component without reflections. The previous mathematical approach is applied for ten frequency points within the rated frequency range of the employed waveguide, considering propagation in both directions. The behaviour for both directions is averaged to obtain the curves shown Figure 3.3. As can be observed for a single curve, the VSWR shows undulations with local minima and maxima; however, this behaviour becomes negligible when considering the total bandwidth. The referenced waveguide dimensions become of importance in later sections of this report; the corresponding dimensions can be found in Table A.2.

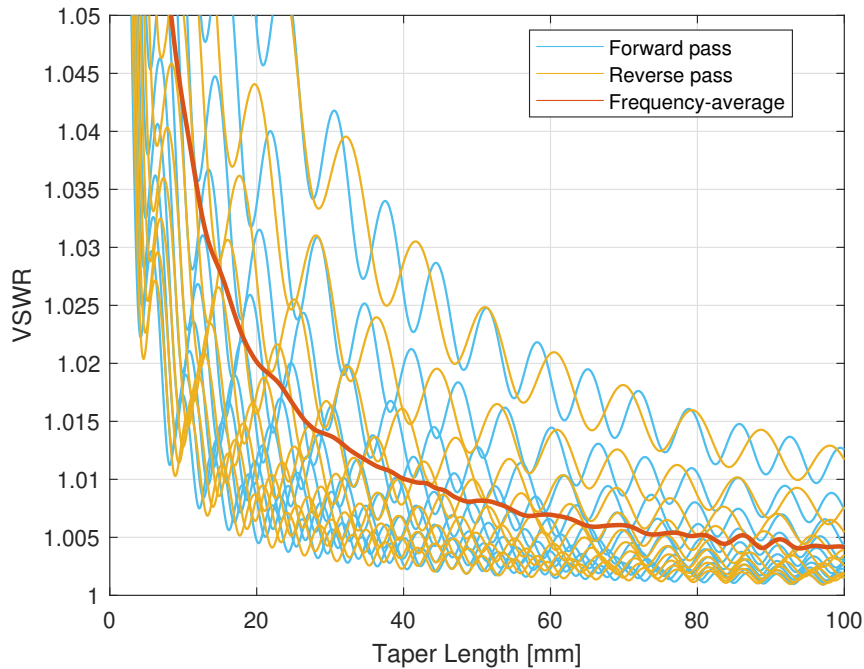


Figure 3.3: Linear waveguide taper VSWR transitioning from COM to WR-28

3.2.2 Non-Linear Taper Profiles

The performance of waveguide tapers can be optimised further using non-linear profiles between the two flanges. One example worth a brief mention is the approach developed by Klopfenstein [5]. An optimal Dolph-Tchebycheff transmission line taper is presented in the sense that it has minimum reflection coefficient magnitude in the passband for a specified length. However, these tapers are not considered any further in this project.

3.2.3 Taper Design Conclusions

For the measurements of this project, exclusively linear taper profiles were used for simplicity, as the design and optimisation of waveguide tapers are not this project's primary focus. Any differences between different profile contours might be overshadowed by manufacturing tolerances and imperfections; therefore, it is more important to focus on proper unterminating and de-embedding techniques (cf. chapter 6). Furthermore, as the waveguide tapers are to be used for measurement applications instead of power transfer, perfect transmission is of lesser importance if the effects can be appropriately de-embedded.

4

Network Analysis

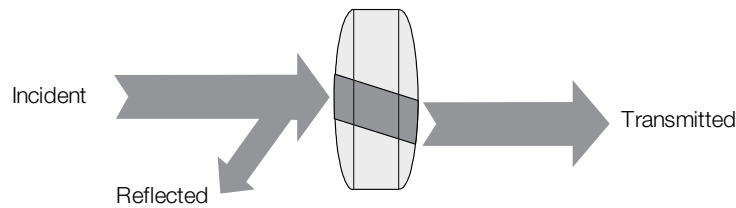


Figure 4.1: Light-wave scattering analogy, reproduced from [6]

In its fundamental form, vector network analysis involves the measurement of incident, reflected, and transmitted waves travelling along transmission lines [6]. An analogy with an optical system can be made: for a light beam incident on a lens, some of the light will be reflected back, whereas some will pass through the lens, as visualised in Figure 4.1. Although the wavelengths are not the same for optical and RF systems, the principle remains the same, with a VNA measuring the incident, reflected, and transmitted energy of a Device Under Test (DUT) [6].

4.1 Wave Parameters

To understand the physical principles behind network analysis, the transmission line model indicated in Figure 4.2 with the corresponding voltages and currents needs to be considered. The total voltage and current on the line are given by the sum of incident and reflected wave amplitudes, shown in Equation 4.1a [1, p. 185], with Z_0 the characteristic impedance of the line. These expressions are solved for the incident and reflected voltage wave amplitudes as shown in Equation 4.1b.

$$\begin{cases} V = V_0^+ + V_0^- \\ I = \frac{1}{Z_0}(V_0^+ - V_0^-) \end{cases} \quad (4.1a) \quad \begin{cases} V_0^+ = \frac{V + Z_0 I}{2} \\ V_0^- = \frac{V - Z_0 I}{2} \end{cases} \quad (4.1b)$$

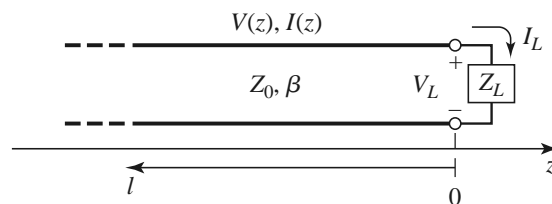


Figure 4.2: Transmission line terminated in load impedance Z_L , reproduced from [1, p. 57]

Given these amplitudes, the concept of *power waves* a and b are introduced, as presented in Equation 4.2 [1, p. 186]. Additionally, the concept may be extended to *pseudo-waves*, which are expressed in Equation 4.3 [7, p. 10]. Z_R represents the reference impedance used for the normalisation of the parameters, which can be chosen independently of the line's physical characteristic impedance. Both wave parameter variants can be used to construct a scattering matrix, resulting in different mathematical properties. Williams presents an extensive comparison of the expressions with their respective differences [8]. Unless stated otherwise, all wave and scattering parameters within this report are based on the power wave formulation by Pozar.

$$\begin{aligned} a_{\text{power}} &= \frac{V + Z_R I}{2\sqrt{\text{Re}(Z_R)}} & a_{\text{pseudo}} &= \sqrt{\text{Re}(Z_R)} \frac{V + Z_R I}{2|Z_R|} \\ b_{\text{power}} &= \frac{V - Z_R^* I}{2\sqrt{\text{Re}(Z_R)}} & b_{\text{pseudo}} &= \sqrt{\text{Re}(Z_R)} \frac{V - Z_R I}{2|Z_R|} \end{aligned} \quad (4.2) \quad (4.3)$$

4.2 Scattering Parameters

Scattering parameters, commonly referred to as S -parameters, are a parameter set that relates to the travelling waves that are scattered or reflected when an n -port network is inserted into a transmission line [7, p. 8-11]. Based on the wave parameters presented in section 4.1, the linear equations describing the n -port network are shown in Equation 4.4a. By definition, each individual S parameter is determined by the ratio between an output and input wave parameter, under the condition that all other input parameters are equal to zero, as shown in Equation 4.4b [7, p. 8-11].

$$\begin{bmatrix} b_1 \\ b_2 \\ \vdots \\ b_n \end{bmatrix} = \begin{bmatrix} S_{11} & S_{12} & \dots & S_{1n} \\ S_{21} & S_{22} & \dots & S_{2n} \\ \vdots & \vdots & \ddots & \vdots \\ S_{n1} & S_{n2} & \dots & S_{nn} \end{bmatrix} \begin{bmatrix} a_1 \\ a_2 \\ \vdots \\ a_n \end{bmatrix} \quad (4.4a) \quad S_{ij} = \frac{b_j}{a_i} \quad a_k = 0, k \neq j \quad (4.4b)$$

This theoretical framework is transposed into practice by combining the significance of the wave parameters with respect to the incident, reflected, and transmitted signals presented at the beginning of the chapter. The wave parameter a always represents the incident signal, whereas the reflected and transmitted signals correspond to the wave parameters b . This allows the definition of a two-port S -parameter measurement as represented in Figure 4.3.

4.2.1 Passivity

In any n -port passive device, the sum of all incoming powers must be greater or equal to the sum of all outgoing powers, leading to the expression shown in Equation 4.5a [9, p. 239]. Equality between the two terms is obtained when the device is both passive and lossless, in which case the expression may be reformulated in terms of the S -parameters as shown in Equation 4.5b [9, p. 240]; with δ_{jk} the Kronecker delta function.

$$\sum_{i=1}^n |a_i|^2 \geq \sum_{i=1}^n |b_i|^2 \quad (4.5a) \quad \sum_{i=1}^n S_{ij}^* S_{ik} = \delta_{jk} \quad (4.5b)$$

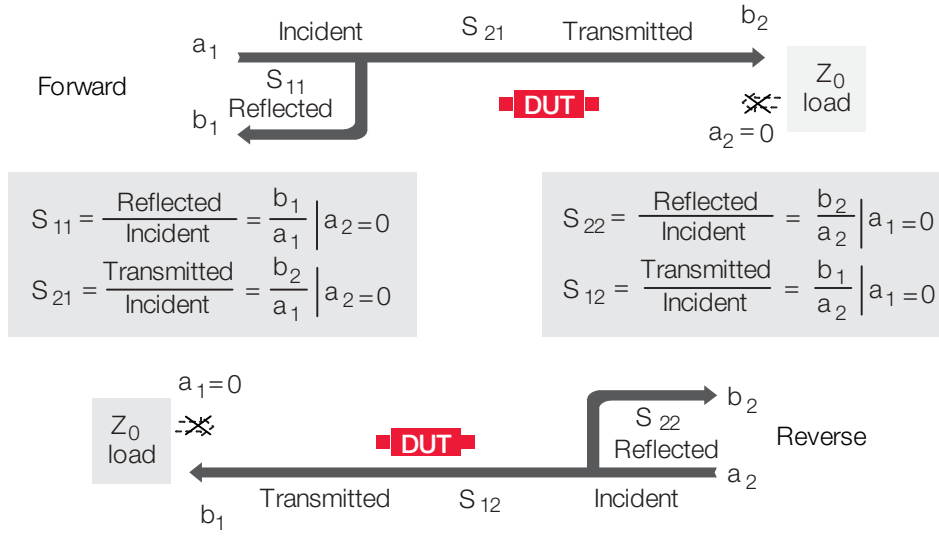


Figure 4.3: S -parameter measurement, reproduced from [6]

4.3 Alternative Expressions & Cascades

The behaviour of a generic two-port device can be expressed by different parameter sets. These include Z (impedance), Y (admittance), h (hybrid), $ABCD$ (chain), S (scattering), and T (chain scattering/transfer) parameters [10]. The developments employed throughout this project are primarily based on S , $ABCD$, or T -parameters. Both $ABCD$ and T -parameter representations can be used for cascading individual two-ports [11]. The $ABCD$ -matrix representation is preferable for waveguide systems, as this representation is agnostic of the characteristic impedances, whereas T -parameters are still based on a reference impedance.

4.3.1 ABCD-Parameters

The $ABCD$ -matrix of a two-port network is defined in terms of the total voltages and currents, satisfying Equation 4.6, with the definition of the voltages and currents shown in Figure 4.4 [1, p. 188-189]. The applicable parameter conversions are shown in section A.3 within Appendix A.

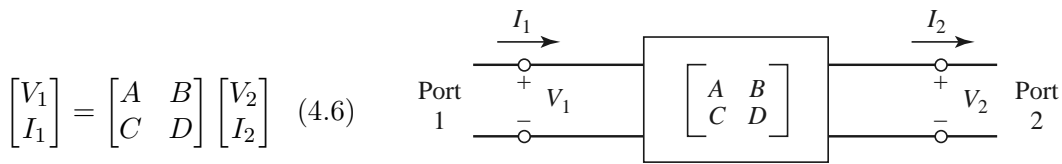


Figure 4.4: $ABCD$ representation, reproduced from [1]

4.3.2 T-Parameters

The T -parameter matrix regroups the information within the S -parameters. The incident and reflected waves are rearranged such that the dependent waves are related to port 1 of the network and independent waves are a function of port 2, satisfying Equation 4.7 [12]. The corresponding transforms are shown in section A.3 within Appendix A.

$$\begin{bmatrix} a_1 \\ b_1 \end{bmatrix} = \begin{bmatrix} T_{11} & T_{21} \\ T_{12} & T_{22} \end{bmatrix} \begin{bmatrix} a_2 \\ b_2 \end{bmatrix} \quad (4.7)$$

Error Models & Calibration

This chapter provides some background on the error models applicable to a Vector Network Analyser (VNA) and the corresponding calibration techniques to reduce the resulting measurement error.

5.1 Error Models

Any measurement system, including a VNA, can be influenced by three main types of measurement errors [13]:

- **Systematic errors**; caused by imperfections in the test equipment and setup
- **Random errors**; varying randomly as a function of time
- **Drift errors**; caused mainly by environmental changes such as temperature variation

Random and drift errors cannot be removed through calibration; systematic errors can be characterised through calibration and mathematically removed from the measurement by the instrument if these errors do not fluctuate over time.

5.1.1 One-Port Error Model

To derive the full two-port error model, a simple one port *error adapter* is considered first, as shown in Figure 5.1. The three systematic error terms are the forward directivity error term E_{df} , the forward reflection tracking error term E_{rf} , and the forward source match error term E_{sf} [12]. The first two terms are caused by non-idealities within the setup, whereas the last term is caused by the impedance mismatch between the instrument and the Device Under Test (DUT). These error terms can be characterised by substituting the DUT by known standards. In the case of a simple SOL calibration, these consist of Short – Open – Load terminations [7, p. 199].

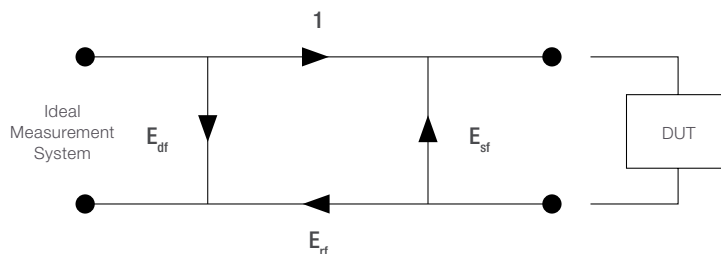


Figure 5.1: One-port error model signal flow graph, reproduced from [12]

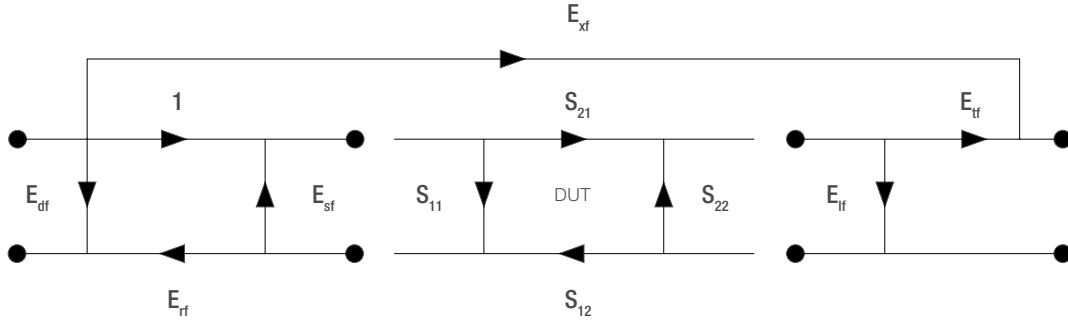


Figure 5.2: Two-port forward error model signal flow graph, reproduced from [12]

5.1.2 Two-Port (Twelve-Term) Error Model

Given the one-port error model, the two-port error model can be constructed, where three additional error terms intervene. These are the forward transmission tracking error term E_{tf} , the forward load match error term E_{lf} , and the forward crosstalk error term E_{xf} ; all illustrated in Figure 5.2. However, this only applies to the forward measurement; adding the reverse measurement (as is required for a complete two-port measurement) leads to the *twelve-term error model* [12] by effectively considering the flow graph of Figure 5.2 for the forward and reverse signal pass. A full two-port calibration of the VNA requires that these error terms are determined over the relevant frequency range for which a DUT is to be measured, although the crosstalk error terms E_{xf} and E_{xr} are almost exclusively neglected.

5.2 Calibration Methods

Calibration is the process of determining the values of the previously established error terms. Different calibration methods have been developed over the years for different applications and with varying accuracy. Some examples which are able to resolve the directivity terms (E_{df} , E_{dr}), tracking terms (E_{rf} , E_{tf} , E_{rr} , E_{tr}), and the matching terms (E_{sf} , E_{lf} , E_{sr} , E_{lr}), include [14, p. 187-189]:

- Through – Open – Short – Match (TOSM)
- Unknown Through – Open – Short – Match (UOSM)
- Through – Open – Match (TOM)
- Through – Short – Match (TSM)
- Through – Reflect – Match (TRM)
- Through – Reflect – Line (TRL)

As all these methods are able to determine the twelve-term error model, with the exception of the crosstalk errors, the choice of calibration is constrained by the type of considered DUT and the overall measurement setup. Especially for waveguide devices, where matched or open terminations are complicated to realise over a wide frequency range, Through – Reflect – Line (TRL) calibration offers a convenient approach with standard waveguide components. Alternatively, calibration may also be performed using an *automatic calibration unit* which is connected to the VNA. The standard method implemented by the

internal electronic components is of type UOSM [14], for the continuation of the project, this is referred to as *ECal* calibration. Table 5.1 compares the two employed calibration methods, the names being synonymous for the calibrated reference planes. How these two calibration methods are of relevance for the measurements performed throughout this project is laid out in section 7.1.

	Manual TRL	ECal
Calibration type	TRL	UOSM
Calibration kit	Waveguide calibration kit	Automatic calibration unit
Reference plane	Waveguide flanges	Coaxial connectors

Table 5.1: Comparison of manual TRL and ECal calibration methods

5.2.1 Through – Reflect – Line (TRL)

In the context of waveguide devices, a TRL calibration requires a short and a shim, meaning a line segment with an electrical length of approximately $\lambda/4$, with λ the geometric centre frequency of the measurement range. The through standard is obtained by directly mating the two waveguide flanges of the reference planes. The length of the line standard (i.e. waveguide shim) must be known approximately, and the magnitude of the reflection coefficient of the reflect standard can be unknown, as long as it is non-zero [14, p. 195-197]. The length of the shim is measured, and the associated delay is computed using Equation 5.1 [15]. The delay values of the used calibration kits are entered in the VNA before calibration. Figure 5.3 presents the three main components necessary for a waveguide TRL calibration: coax-to-WG adapter, waveguide short, and waveguide shim.

$$\frac{\text{length of } 1/4 \text{ wavelength section [mm]}}{299.6953 \text{ mm/ns (propagation velocity in air)}} = \text{offset delay [ns]} \quad (5.1)$$

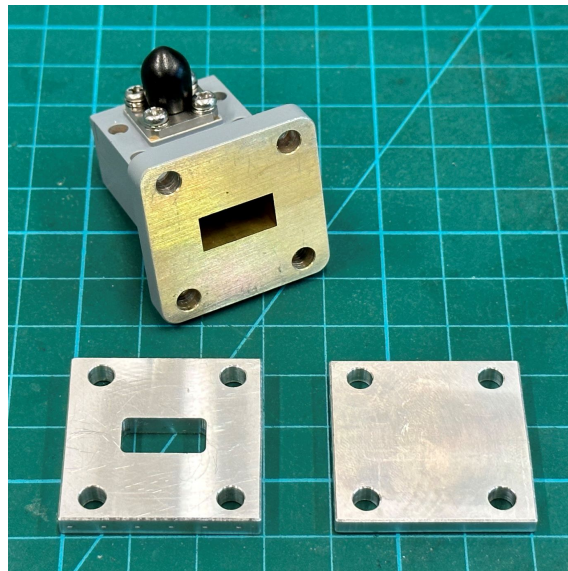


Figure 5.3: WR-51 manual TRL calibration kit including shim and short for through, line, and reflect measurements

The complete derivation of the error terms for a TRL calibration can be looked up as presented by Soares, Gouzien, Legaud *et al.* [16] or by Ferrero [7, p. 208-210]. Furthermore, Juroshek, Hoer and Kaiser demonstrate that large imperfections in the test ports of the VNA, and by extension, in the coax-to-WG adapters, especially related to impedance mismatches, can be tolerated if proper calibration procedures are used [17]. In subsequent de-embedding operations, only the waveguide components intervening in-between the coax-to-WG adapters and the DUT need to be de-embedded given a manual TRL calibration.

5.2.2 Unknown Through – Open – Short – Match (UOSM)

The UOSM calibration method, also referred to as Short – Open – Load – Through (SOLT), can be performed by an automatic calibration unit, also referred to as Electronic Calibration (ECal). Ferrero presents the mathematical derivation of the error terms [7, p. 215-216]. In the context of this project, such a calibration is exclusively performed on the connectors of the coaxial cables of the VNA. Therefore, the coax-to-WG adapters and the waveguide fixtures must be de-embedded after this calibration. Generally, automatic calibration is faster and more secure than manual calibration for several reasons [14, p. 206-207]:

- There is no need to connect several standards manually.
- Invalid calibrations due to operator errors are almost excluded.
- No need to handle calibration kit data.
- The internal standards do not wear out as they are switched electronically.

5.3 Fixture Compensation

In addition to the standard calibration methods, the used VNA has an additional feature referred to as *fixture compensation*. Fixture compensation can be beneficial if the reference plane of the calibration cannot be placed directly at the DUT ports, for example, because the DUT has non-coaxial ports and can only be measured in a test fixture. Fixture compensation is an automated length offset and loss compensation for test fixtures; it complements a previous calibration and replaces a possible manual length offset and loss correction [14, p. 232-233]. It is essential to choose *direct compensation* for a frequency-dependent transmission factor, as the loss of the fixtures is not constant with frequency. The compensating terms are determined by the VNA, by terminating the ports at the ends of the fixtures with a short and/or open. Only one termination is used for waveguide devices: a shorting plate covering the waveguide flange.

5.4 Further Remarks

An excellent derivation of various error models and the corresponding uncertainties is presented by Rytting [18]. Furthermore, sophisticated techniques may be taken into account to compensate for the effects of misaligned waveguide flanges in the calibration process [19], as this becomes of greater importance when increasing the frequency; nevertheless, such approaches were deemed too complex for this particular project. An additional discussion on the influence of mismatches caused by waveguide tolerances and misalignment is presented by Kerr [20].

6

Unterminating & De-Embedding

When discussing procedures to obtain the behaviour of a Device Under Test (DUT), embedded within a test structure (i.e. the DUT reference planes do not coincide with the calibration reference planes), two distinct problems need to be studied. These two terms are often confounded in literature but represent problems distinct from each other:

- **Unterminating**

Unterminating refers to deducing the behaviour of the embedding structure (e.g. waveguide tapers) from compounded measurements. This is necessary when no prior knowledge about the behaviour of the embedding structure is available. *It is the process of deducing the properties of the intervening structure from a series of measurements with known embedded devices* [21].

- **De-Embedding**

De-embedding refers to extracting the contribution of the DUT when embedded in a test network. This requires knowledge about the behaviour of the embedding structure obtained through unterminating or other means. *It is the process of deducing the impedance of a device under test from measurements made at a distance when the electrical properties of the intervening structure are known* [21].

The conjunction of these two problems was solved in the context of different setups, validating and comparing the developed algorithms and approaches. Figure 6.1 shows the general signal flow graph of a DUT embedded within a test structure with fixtures A and B. Unterminating consists of determining the values of FA_{ij} and FB_{ij} , whereas de-embedding consists of determining S_{ij} , given FA_{ij} and FB_{ij} .

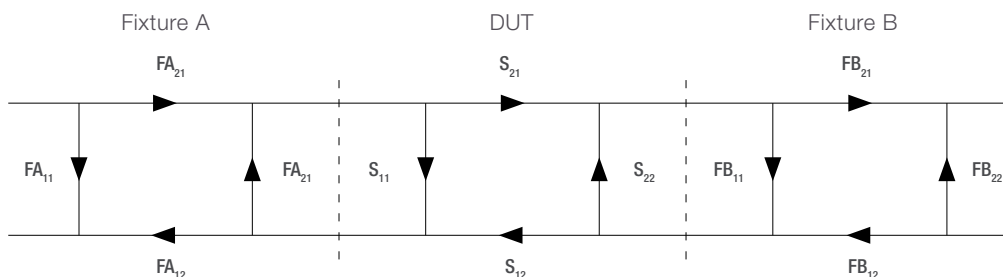


Figure 6.1: Signal flow graph of the test fixtures and DUT, reproduced from [12]

6.1 Relation to Error Models

Indeed, the signal flow graph of a DUT embedded within a set of fixtures as shown in Figure 6.1 bears some resemblance with the twelve-term error model shown in Figure 5.2. A complete flow graph can be established, including the cascade of the fixtures and the DUT as shown in Figure 6.2. The original error terms can be cascaded with the S -parameters of the fixtures to obtain new error terms with the forward error terms computed in Equation 6.1 and the reverse error terms computed in Equation 6.2. Therefore, the unterminating/de-embedding operation is equivalent to establishing a new calibrated reference plane via the twelve-term error model.

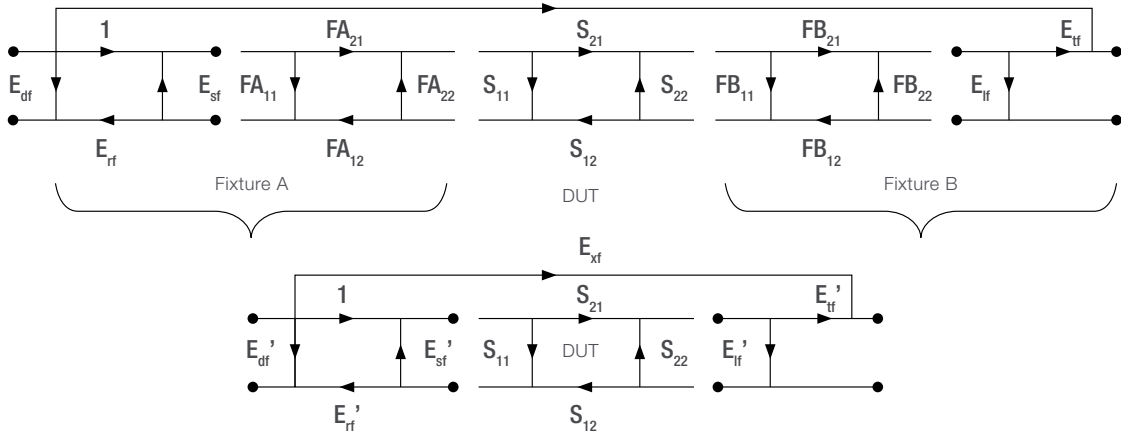


Figure 6.2: Signal flow graph of the combined test setup with forward error terms, reproduced from [12]

$$E_{df}' = E_{df} + \frac{E_{rf} FA_{11}}{1 - E_{sf} FA_{11}} \quad (6.1a)$$

$$E_{sf}' = FA_{22} + \frac{E_{sf} FA_{12} FA_{21}}{1 - E_{sf} FA_{11}} \quad (6.1b)$$

$$E_{rf}' = \frac{E_{rf} FA_{12} FA_{21}}{1 - E_{sf} FA_{11}} \quad (6.1c)$$

$$E_{lf}' = FB_{11} + \frac{E_{lf} FB_{12} FB_{21}}{1 - E_{lf} FB_{22}} \quad (6.1d)$$

$$E_{tf}' = \frac{E_{tf} FA_{21} FB_{21}}{(1 - E_{lf} FB_{22})(1 - E_{sf} FA_{11})} \quad (6.1e)$$

$$E_{xf}' = E_{xf} \quad (6.1f)$$

$$E_{dr}' = E_{dr} + \frac{E_{rr} FB_{22}}{1 - E_{sr} FB_{22}} \quad (6.2a)$$

$$E_{sr}' = FB_{11} + \frac{E_{sr} FB_{12} FB_{21}}{1 - E_{sr} FB_{22}} \quad (6.2b)$$

$$E_{rr}' = \frac{E_{rr} FB_{12} FB_{21}}{1 - E_{sr} FB_{22}} \quad (6.2c)$$

$$E_{lr}' = FA_{22} + \frac{E_{lr} FA_{12} FA_{21}}{1 - E_{lr} FA_{11}} \quad (6.2d)$$

$$E_{tr}' = \frac{E_{tr} FA_{12} FB_{12}}{(1 - E_{lr} FA_{11})(1 - E_{sr} FB_{22})} \quad (6.2e)$$

$$E_{xr}' = E_{xr} \quad (6.2f)$$

6.2 Unterminating

Different measurement techniques can be used for the unterminating operation. The most general approach, which is also the most adapted to waveguide devices, is referred to as *2x-thru de-embedding*, a technique which is also applicable to unsymmetrical test fixtures [22]. Two identical fixtures are cascaded without the DUT, and the measurement is bisected mathematically afterwards. If the DUT is embedded in an asymmetric test structure (such as shown in Figure 6.1), both are measured and bisected independently. Different methods

are proposed for the measurement bisection; the corresponding MATLAB implementations are presented in Listing C.2. Given that bisection is equivalent to solving the matrix equation $A = BB$ for B , with A the $ABCD$ matrix of the 2x-thru measurement and B the $ABCD$ matrix of an individual fixture, unterminating becomes a mathematical problem of determining the matrix square root.

6.2.1 Matrix Diagonalisation

The standard procedure for computing the square root of a matrix A is to diagonalise A , such that there exists an invertible eigenvector matrix P and a diagonal eigenvalue matrix D satisfying $P^{-1}AP = D$ [23]. The overall square root is obtained by computing the square roots of the individual eigenvalues within D . The expression in Equation 6.3 is obtained, with P and D , the matrix of eigenvectors and eigenvalues of A_{2xA} , respectively. This method allows forcing the computation of real eigenvalues, the consequences of which are discussed in section 8.1.

$$A_A = (A_{2xA})^{1/2} = PD^{1/2}P^{-1} \quad (6.3)$$

6.2.2 Schur Decomposition

Similar to the standard matrix diagonalisation procedure, the Schur decomposition of a matrix may be computed. This method extends the notion of matrix square root for cases where the matrix of interest may not be diagonalisable. The Schur decomposition satisfies $A = QTQ^*$, with T upper triangular and Q unitary matrices [24]. The expression in Equation 6.4 is obtained, with T and Q , the matrices derived from A_{2xA} . This method is implemented in MATLAB by the `sqrtn` function, suggested for this specific use case [25].

$$A_A = (A_{2xA})^{1/2} = QT^{1/2}Q^* \quad (6.4)$$

6.2.3 Input Parasitics

A more physical approach is proposed by Simion [26], [27], specifically applied to coax-to-waveguide transitions. First, an equivalent circuit model for the 2x-thru measurement is established as presented in Figure 6.3. The two-port input circuits C_{in} of the overall equivalent circuit are of particular importance, as they congregate all losses of the structure. Next, the $ABCD$ matrices A_{thru} of the 2x-thru measurement are converted to Z -parameters to obtain Z_{thru} , and a matrix $Z_x = j \cdot \text{imag}(Z_{thru})$ is computed, which is converted back into the $ABCD$ matrix A_x . Subsequently, a cascade is established, from where the $ABCD$ matrix A_{in} is to be extracted as shown in Equation 6.5 (cf. [28] for the computation of this matrix equation). As shown, the solution of the matrix equation uses the matrix square root and therefore requires the Schur decomposition presented in subsection 6.2.2.

$$A_{thru} = A_{in}A_xA_{in} \Leftrightarrow A_{in} = (A_x)^{-1/2}((A_x)^{-1/2}A_{thru}(A_x)^{-1/2})^{-1/2}(A_x)^{-1/2} \quad (6.5)$$

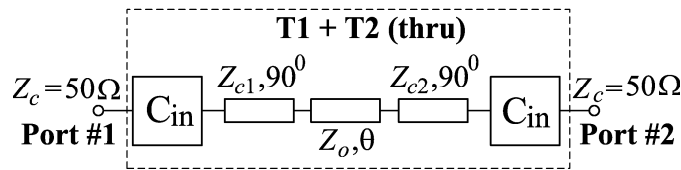


Figure 6.3: 2x-thru measurement equivalent circuit model, reproduced from [26]

The complete method includes further steps; however, these were found not of relevance to the studied problems. Mainly because all losses are attributed to the input circuits with the additional steps correcting for the phase delay of the system. Although it would have been of interest to study the proposed algorithm in its entirety, the steps laid out in the two relevant references [26], [27] could not be reproduced successfully.

6.2.4 Alternative Unterminating Approaches

Time-gating is often used in the context of unterminating procedures and provides the ability to selectively remove or include responses in time on the VNA [29]. Van Hauwermeiren, Botte and De Zutter propose the use of gating to increase the accuracy of the 2x-thru measurement [30]. Another approach presented by Dunsmore, Cheng and Zhang is to use time-gating for 2x-thru measurements of asymmetric test fixtures [31]. The behaviour of the two fixtures can be separated by only maintaining the measurement response within a relevant time window. However, this requires that the two fixtures are mechanically compatible and have an equal electrical length and insertion loss.

Other methods not based on a 2x-thru measurement may also be considered. The transmission matrix of a liner double taper can be determined analytically, for example, using the approach presented by Chakraborty and Sanyal [32]. Some analyses arrive at the conclusion that the fundamental and first higher-order mode within a taper can be represented as ideal lossless transmission lines [33], effectively making de-embedding unnecessary if only the amplitudes of the signals are considered. However, this hypothesis does not hold up to the measurements presented in this project.

6.3 De-Embedding

Coming back to the signal flow graph of Figure 6.1, de-embedding becomes a purely mathematical process after the behaviour of the embedding structure has been determined through unterminating or other means. The process can be summarised in the following five steps [34], with the main de-embedding equation implemented in Listing C.3:

- i) 2x-thru measurement of fixture A and conversion to $ABCD$ -parameters:

$$A_{2xA} = A_A A_A \quad (6.6a)$$

- ii) 2x-thru measurement of fixture B and conversion to $ABCD$ -parameters:

$$A_{2xB} = A_B A_B \quad (6.6b)$$

- iii) Computation of the individual $ABCD$ matrices A_A and A_B (i.e. unterminating)

- iv) Deduction of the full-path cascade equation:

$$A_{\text{cascade}} = A_A A_{\text{DUT}} A_B \quad (6.6c)$$

- v) Inversion of the cascade equation to obtain the DUT $ABCD$ matrix A_{DUT} and conversion to S -parameters:

$$A_{\text{DUT}} = A_A^{-1} A_{\text{cascade}} A_B^{-1} \quad (6.6d)$$

Nevertheless, the conversion to $ABCD$ or T -parameters followed by the inverse operation is not required for all de-embedding methods. Scafati, Paulis, Olivieri *et al.* present a method which avoids these steps and performs the entire de-embedding operation only using S -parameters [35]. Although this technique is more complicated in the two-port case, it renders de-embedding for DUTs with a large number of ports mathematically simpler. Furthermore, the 2x-thru measurements can be complemented with simulations of the embedding structures: Wang, Jin, Bird *et al.* propose a hybrid de-embedding approach, merging measurement and simulation data to either obtain similar de-embedding accuracy with fewer test structures or better accuracy with the same test structures [36]. Although this approach is geared towards microstrip line structures on PCBs, it presents an interesting framework that may also be of interest for more complex waveguide devices.

6.3.1 Standardised Procedures

IEEE standard 370 [37] was defined with the goal of providing a consistent framework for de-embedding techniques, mainly for Printed Circuit Board (PCB) applications. The full algorithm is presented by Ellison, Smith and Agili [38] and relies on time-gating for separation of the error terms caused by the two individual fixtures in a 2x-thru measurement. As an extension, the same authors propose to include impedance correction in a later publication to increase the robustness of the proposed method [39]. Although open-source implementations of IEEE-370, including impedance correction, are available [40], these proved difficult to implement with the waveguide measurements studied in this project, especially as the standard has not been defined with waveguide devices in mind.

6.3.2 Commercial Software

In addition to previously explained methods, unterminating/de-embedding may also be accomplished through commercial software. Examples include EaZy De-Embedding (EZD) as an implementation of IEEE 370, Advanced Interconnect Test Tool (AITT) by Clear Signal Solutions [41], or In-Situ De-Embedding (ISD) by AtaiTec [42]. These software packages may be installed and used directly on the VNA [14, p. 301-303], given the proper licenses. The main disadvantage of these options is that they all represent black boxes to some extent, as they integrate proprietary algorithms which cannot be replicated externally [22]. Additionally, their licensing costs may be prohibitive if only a low number of measurements is required. Nevertheless, the results obtained with AITT have been compared to other techniques through a trial license as shown in subsection 7.2.3.

6.4 Port Augmentation

As briefly mentioned in the introduction, the studied diplexer is a three-port device. Therefore, an adequate measurement approach must be defined to fully characterise its S -parameters using the available 2-port VNA. In an ideal measurement setup, the third port would have to be perfectly matched for the full range of frequencies for which the measurements are established. This can be easily achieved on coaxial devices where the reference impedance in most cases is equal to $50\ \Omega$, independent of the frequency. This approach becomes more complicated in waveguide components, as the impedance is close to the vacuum impedance Z_0 and varies with frequency, asymptotically approaching an infinite impedance close to the cutoff frequency of the waveguide (cf. subsection 3.1.3). Independently of the chosen method in constructing three-port measurements, the combination of the individual two-port S -parameter matrices will lead to an overdetermined system of equations, as the final reflective terms S_{11} , S_{22} , and S_{33} will have been determined by two separate measurements each, as illustrated in Equation 6.7.

$$\begin{bmatrix} S_{11}|S_{11} & S_{12} & S_{13} \\ S_{21} & S_{22}|S_{22} & S_{23} \\ S_{31} & S_{32} & S_{33}|S_{33} \end{bmatrix} \Leftarrow \begin{cases} \begin{bmatrix} \cdot \\ b_2 \\ b_3 \end{bmatrix} = \begin{bmatrix} \cdot & \cdot & \cdot \\ \cdot & S_{22} & S_{23} \\ \cdot & S_{32} & S_{33} \end{bmatrix} \begin{bmatrix} \cdot \\ a_2 \\ a_3 \end{bmatrix} & \text{Port 1 terminated} \\ \begin{bmatrix} b_1 \\ \cdot \\ b_3 \end{bmatrix} = \begin{bmatrix} S_{11} & \cdot & S_{13} \\ \cdot & \cdot & \cdot \\ S_{31} & \cdot & S_{33} \end{bmatrix} \begin{bmatrix} a_1 \\ \cdot \\ a_3 \end{bmatrix} & \text{Port 2 terminated} \\ \begin{bmatrix} b_1 \\ b_2 \\ \cdot \end{bmatrix} = \begin{bmatrix} S_{11} & S_{12} & \cdot \\ S_{21} & S_{22} & \cdot \\ \cdot & \cdot & \cdot \end{bmatrix} \begin{bmatrix} a_1 \\ a_2 \\ \cdot \end{bmatrix} & \text{Port 3 terminated} \end{cases} \quad (6.7)$$

6.4.1 Impedance Renormalisation

One possibility for accurate multiport measurements on a two-port VNA is described by Tippet and Speciale [43]. Using the proposed method, the measurement of an n -port device requires n separate auxiliary loads. A scattering matrix renormalisation is performed, which requires that none of the employed loads is perfectly reflecting. With all n loads attributed to one of the n ports of the DUT, the renormalisation is computed as shown in Equation 6.8, with S the scattering matrix with the n auxiliary loads, Γ the matrix with the reflection coefficients of the n auxiliary loads on its diagonal, I the identity matrix, and S' the renormalised scattering matrix. All matrices are of dimension n by n .

$$S' = (I - S)^{-1}(S - \Gamma)(I - S \cdot \Gamma)^{-1}(I - S) \quad (6.8)$$

Although this may seem like a simple approach in theory, the application to waveguide devices becomes more complicated. Assuming that auxiliary loads with impedances Z_i are used for termination, the reflection coefficients Γ_i can only be determined using the frequency-dependent characteristic impedances of the waveguide ports using Equation 6.9 [1, p. 57]. If, in turn, the auxiliary loads are defined in terms of their expected reflection coefficients (e.g. -0.9 for a non-perfect shorting plate), these values need to be renormalised as a function of the waveguide port impedance; otherwise the computation of S' will be skewed if the different ports possess different characteristic impedances, as is the case for the studied diplexer.

$$\Gamma = \frac{Z_L - Z_0}{Z_L + Z_0} \quad (6.9)$$

6.4.2 Wave Identification

As an extension to the impedance renormalisation method, Rolfes and Schiek propose a method based on the wave parameters a and b (cf. section 4.1) of the measurement [44], referred to as the *wave-identification method* in a later publication [45]. This method is based on the solution of the matrix equation shown in Equation 6.10, where m_i^j indicates the known i -th output wave parameter of the j -th measurement, a_i^j the known i -th input wave parameter of the j -th measurement, and Γ_i the terminating reflection coefficients. As this formulation includes nine variables (the S -parameters to be determined) but only six off-diagonal equations that can be evaluated, a second set of input wave parameters \tilde{a}_i^j with corresponding output wave parameters \tilde{m}_i^j are defined, with the requirement that a and \tilde{a}

are orthogonal to each other and that \vec{a}^j ($j = 1, 2, 3$) as well as $\vec{\tilde{a}}^j$ ($j = 1, 2, 3$) form linearly independent bases of the same vector space. In practice, this requirement translates into that for a , the VNA only transmits on the first of its physical ports (i.e. measuring S_{11} and S_{21}), whereas, for \tilde{a} , the VNA only transmits on the second of its physical ports (i.e. measuring S_{12} and S_{22}). This leads to a system of twelve equations with nine unknowns, allowing for the S -parameters to be computed. Again, this system is overdetermined, the parameters S_{ii} ($i = 1, 2, 3$) being characterised by two equations each. The full derivation is not detailed here (cf. the original publication by Rolfes and Schiek [44]); nevertheless, computation of the parameters b_1^1, b_2^2, b_3^3 allows for the computation of the full 3-by-3 S -parameter matrix using Equation 6.10. The corresponding implementation in MATLAB is presented in Listing C.4.

$$\begin{bmatrix} b_1^1 & m_1^2 & m_1^3 \\ m_2^1 & b_2^2 & m_2^3 \\ m_3^1 & m_3^2 & b_3^3 \end{bmatrix} = \begin{bmatrix} S_{11} & S_{12} & S_{13} \\ S_{21} & S_{22} & S_{23} \\ S_{31} & S_{32} & S_{33} \end{bmatrix} \begin{bmatrix} \Gamma_1 b_1^1 & a_1^2 & a_1^3 \\ a_2^1 & \Gamma_2 b_2^2 & a_2^3 \\ a_3^1 & a_3^2 & \Gamma_3 b_3^3 \end{bmatrix} \quad (6.10)$$

Measurements

Two classes of devices by MinWave have been characterised: double-ridged waveguides for the validation of the unterminating/de-embedding techniques laid out in section 6.2 and section 6.3, respectively, as well as a three-port diplexer to validate the previous techniques and supplement them with the multi-port measurement techniques presented in section 6.4.

7.1 Calibration Methods

Measurements were performed using two calibration methods, hereafter referred to as *manual TRL* and *ECal*, previously presented in section 5.2. These terms are used synonymously for the calibrated reference planes; TRL signifying a calibration between the waveguide flanges of the coax adapters, ECal denoting a calibration between the end connectors of the coax cables leading to the VNA. Therefore, the fixture to be de-embedded only includes the waveguide tapers in the former case, whereas in the latter case, the tapers and the coax-WG adapters are to be de-embedded. As stated previously, these two calibration planes were compared, as the ECal method avoids the use of waveguide calibration kits, which may simplify the measurement process.

7.2 Double-Ridged Waveguides

Double-ridged waveguide passband filters with a WRD-750 flange (cf. Nickel [46]) were studied. These flanges are coupled to the WR-75 coax adapters using tapers designed by MinWave. The subsequent analyses focus on MW13200 as the filter and MW33401 as the taper. These two components are represented in Figure 7.1. As a cascade of three two-port devices, illustrated in Figure 7.2a, this is the ideal test setup for unterminating and de-embedding, adhering to the signal flow graph presented earlier in Figure 6.1. The corresponding setup for the 2x-thru measurement is shown in Figure 7.2b, and the physical assemblies are illustrated in Figure 7.3.



(a) MinWave MW13200 filter

(b) MinWave MW33401 taper interior

Figure 7.1: Double-ridged waveguide components

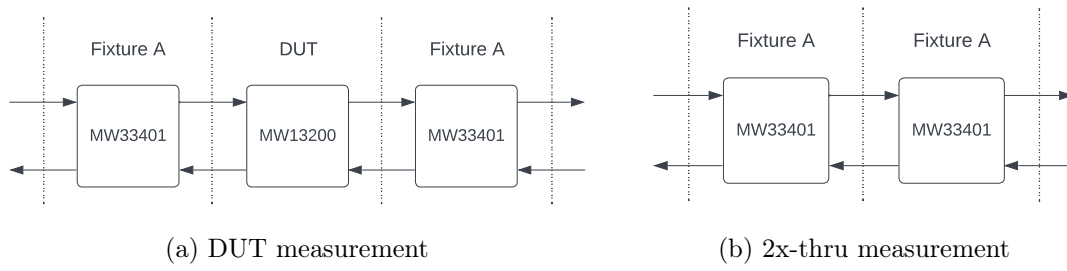


Figure 7.2: Schematic measurement setups of the embedded DUT

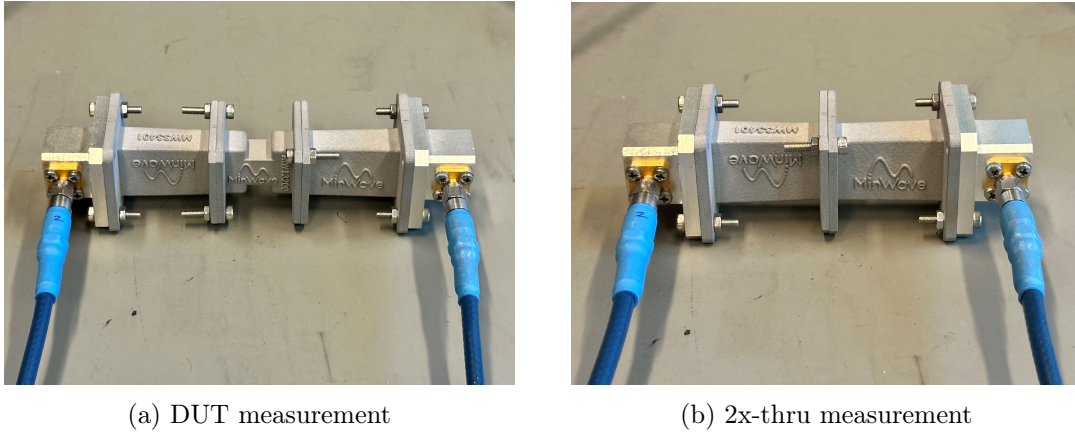


Figure 7.3: Photos of the filter measurement setups represented in Figure 7.2

7.2.1 Measurement Baseline

All of the subsequently presented post-processing steps have the embedded (i.e. non-de-embedded) measurements as a starting point. These measurements correspond directly to the data obtained from the VNA and are shown in Figure 7.4. In addition, the end results can be compared to the component's behaviour as expected from simulation, shown in Figure 7.5.

7.2.2 Bisection Comparison

In a first step, different techniques of obtaining the bisected fixture behaviour from the 2x-thru measurement are studied, as laid out in section 6.2. Comparisons of the effects on S_{21} and S_{11} due to the different methods are shown in Figure 7.6a and Figure 7.6b, respectively. The individual measurements are displayed in Figure B.3 within Appendix B. It can be observed that the different methods perform similarly in terms of the general outline; however, some numerical instabilities can be observed for the Schur decomposition and input parasitics methods. It is important to note that this is not a physical effect but is entirely due to the way that the square root of a complex number is defined and computed (cf. section 8.1). Therefore, the most stable technique is the simple matrix diagonalisation with forced real square roots (cf. subsection 6.2.1). Unless stated otherwise, this method is used for the processing of all following measurements.

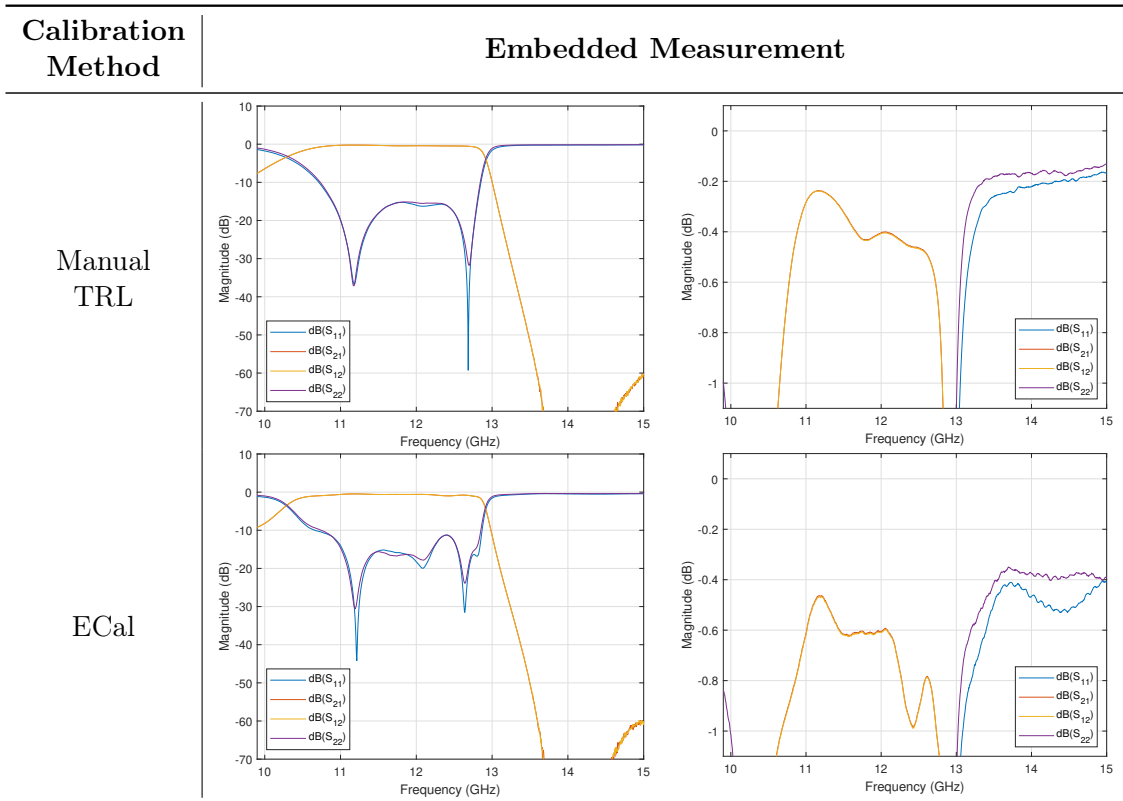


Figure 7.4: MW13200 embedded magnitude S -parameter measurements

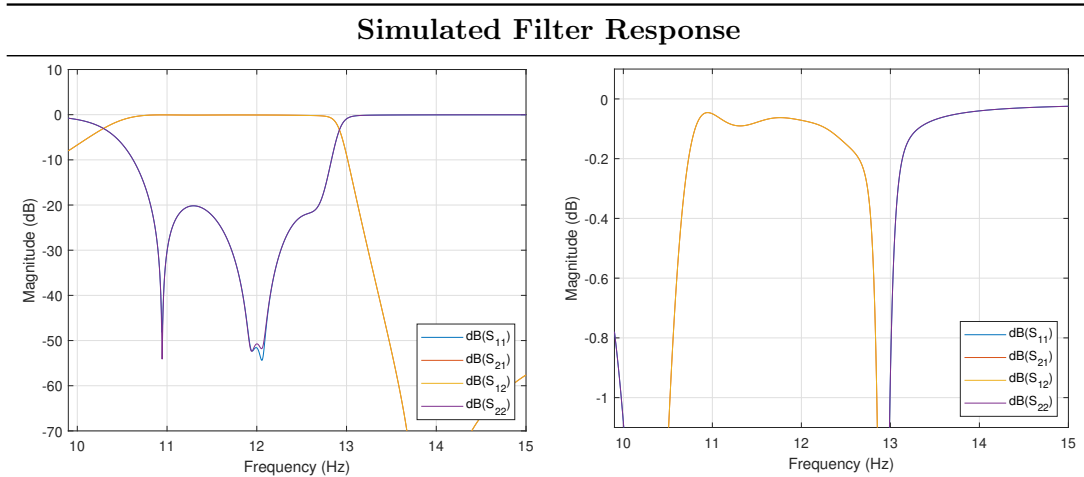
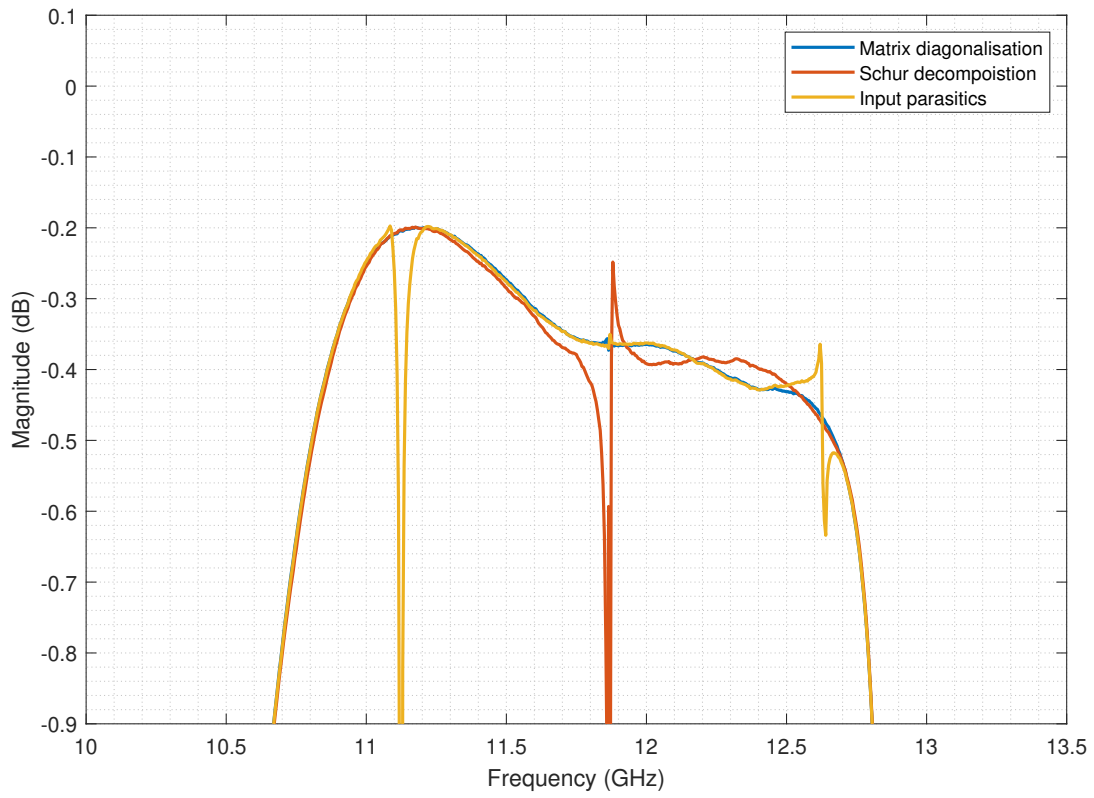
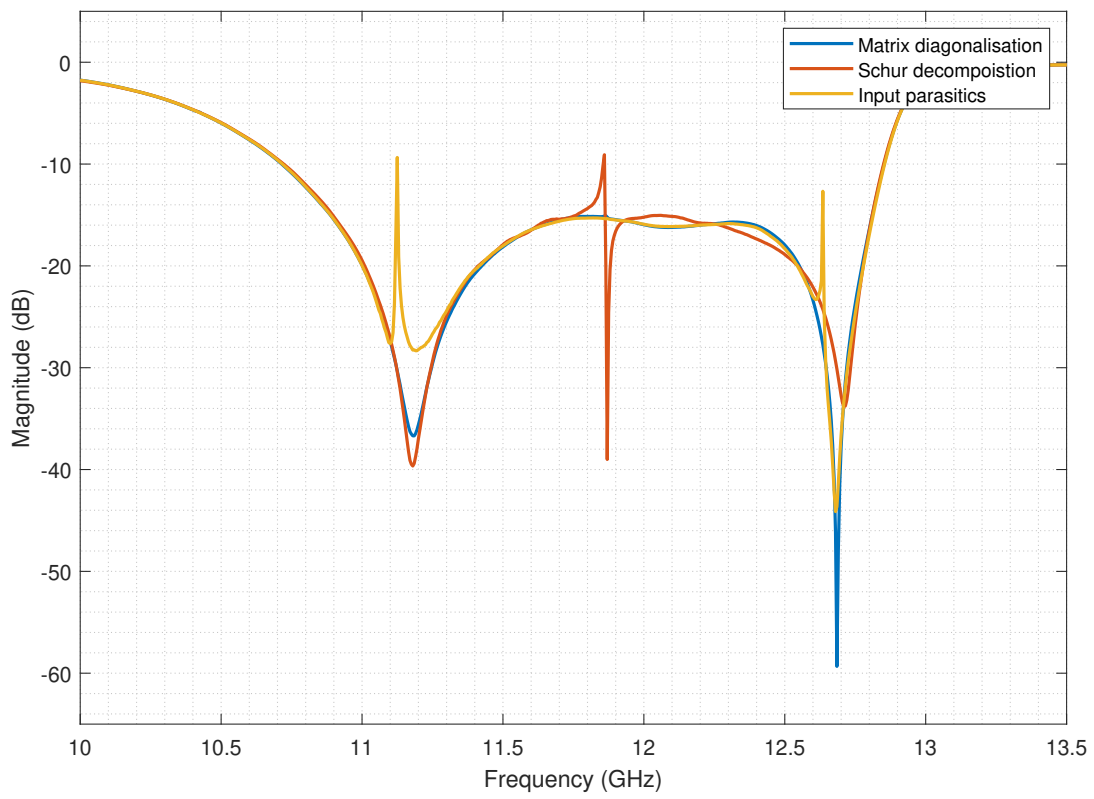


Figure 7.5: MW13200 simulated magnitude S -parameters



(a) Injecton loss S_{21}



(b) Return loss S_{11}

Figure 7.6: Comparison of manual TRL bisection methods

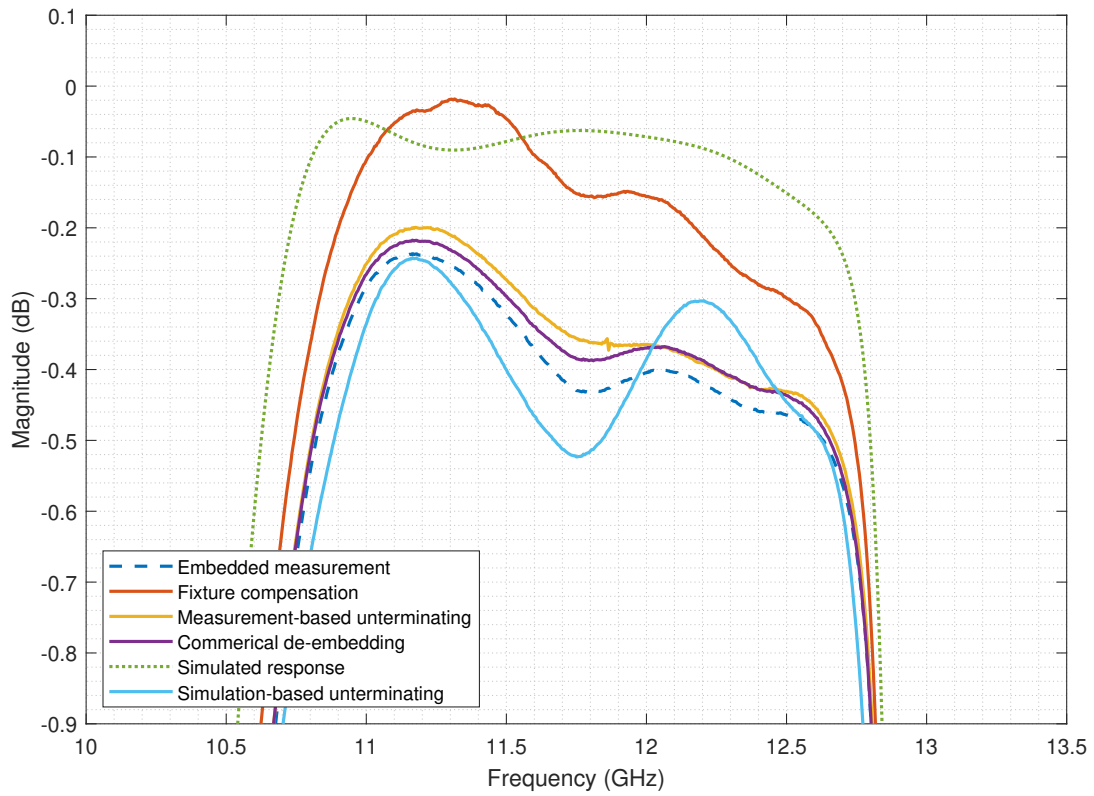
7.2.3 Method Comparison

In a second step, different methods of unterminating/de-embedding are studied for both manual TRL and ECal calibrations. These include de-embedding with the unterminated tapers and de-embedding through fixture compensation (cf. section 5.3). Both of these methods rely on the measurement of the waveguide tapers and can therefore account for the non-ideal behaviour of the tapers. Furthermore, if the measurement setup is calibrated between the waveguide flanges of the adapters (i.e. manual TRL calibration), the behaviour of the tapers can also be obtained through simulation. Although this requires one less measurement, it may prove problematic if the tapers perform differently than anticipated by simulation. Commercial software may also be used for unterminating/de-embedding (subsection 6.3.2) with the Advanced Interconnect Test Tool (AITT) [41] used as a reference. Table 7.1 briefly summarises the possible combinations of the possible unterminating/de-embedding methods. Simulation-based unterminating is not possible for ECal measurements, as this would require a simulation model of the employed coax-WG adapters. The individual measurements are shown in Figure B.1 and Figure B.2 within Appendix B.

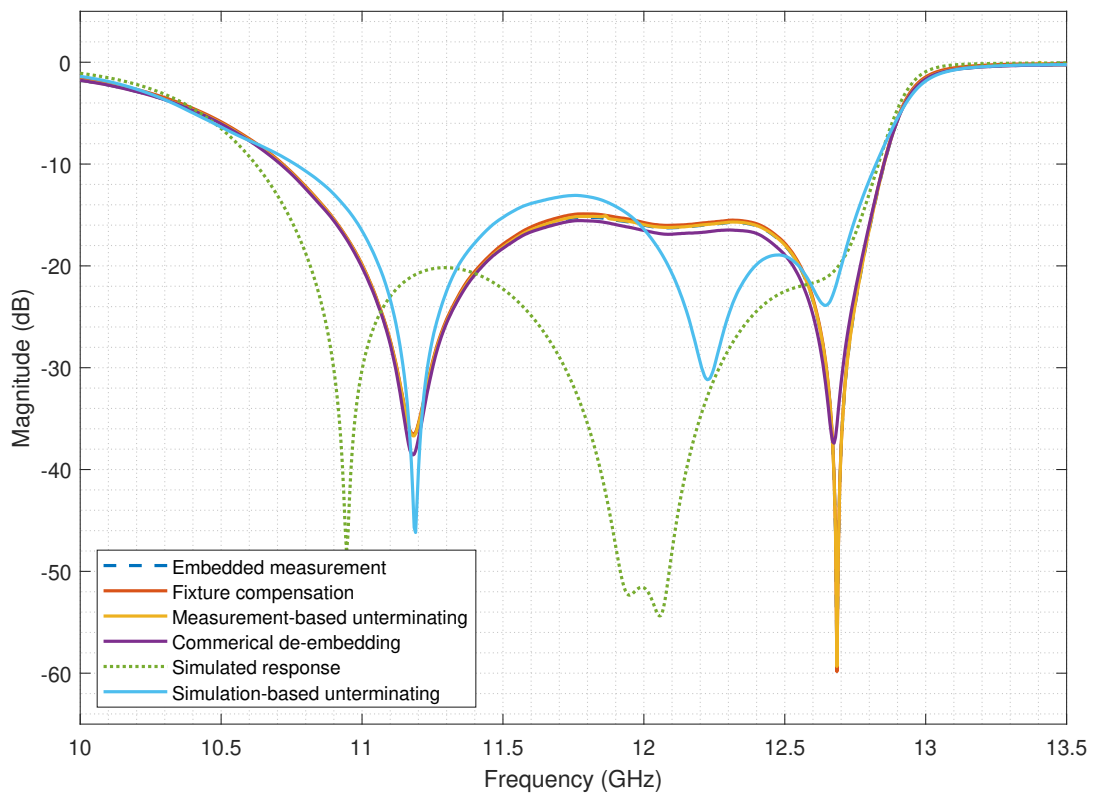
Calibration Method	Measurement-Based Unterminating	Simulation-Based Unterminating	Fixture Compensation	Commercial Software
Manual TRL	✓	✓	✓	✓
ECal	✓	✗	✓	✓

Table 7.1: Unterminating/de-embedding method comparison

For both manual TRL and ECal, data obtained via measurement-based unterminating and through commercial solutions coincide within 0.05 dB for S_{21} within the passband, proving the validity of the developed method. Fixture compensation tends to overcompensate the losses, which may lead to erroneous conclusions about the Device Under Test (DUT). Simulation-based unterminating also shows some discrepancies with the other methods but may be used as an approximation if 2x-thru measurements can not be performed due to the geometry of a particular DUT. Furthermore, in Figure 7.7b can be observed how the peaks of S_{11} for the simulation-based unterminating technique appear as a combination of measurement and simulation results, indicating the hybrid nature of this technique. Comparing the manual TRL and ECal calibration methods, it can be observed that much smoother results are obtained for S_{21} when calibrating the VNA at the waveguide flanges; however, calibration at the exterior of the waveguides may still be acceptable under certain conditions when a waveguide calibration kit is not available, although the de-embedding also tends to overcompensate the losses of the fixtures. With regards to S_{11} , the difference between the two calibration planes/methods becomes much more apparent, indicating that for accurate measurements of this parameter, manual TRL calibration between the waveguide flanges is preferable.

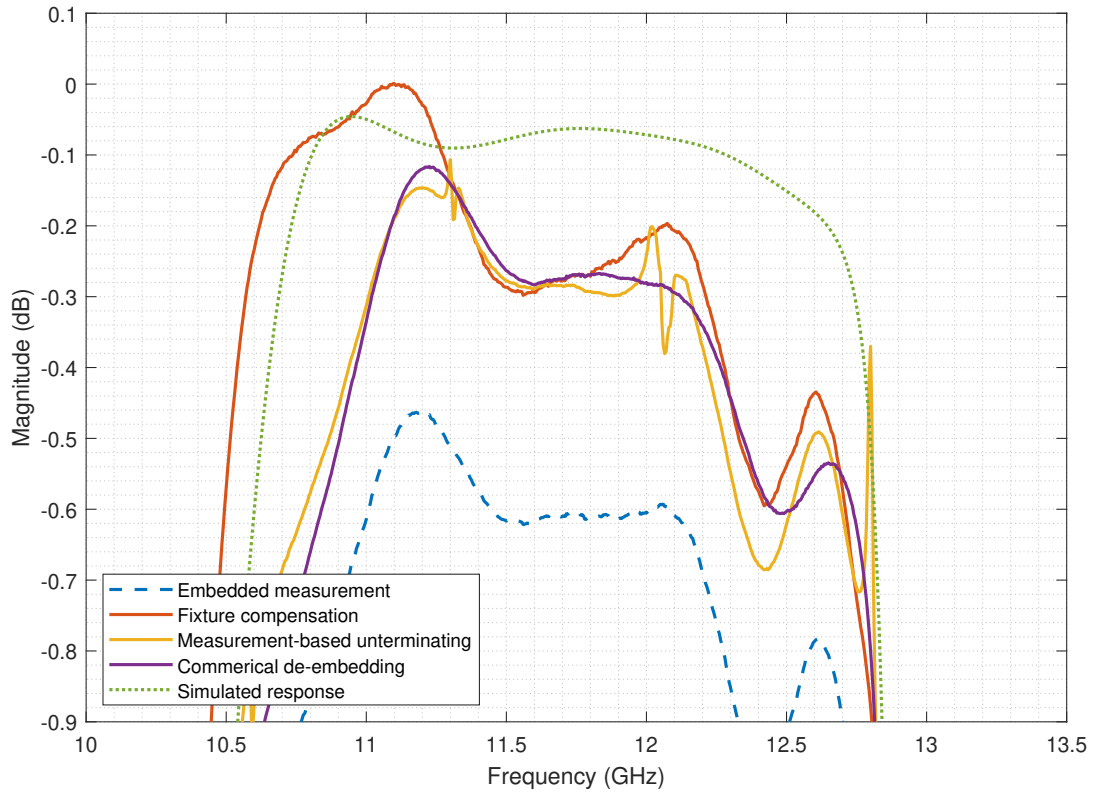


(a) Injecton loss S_{21}

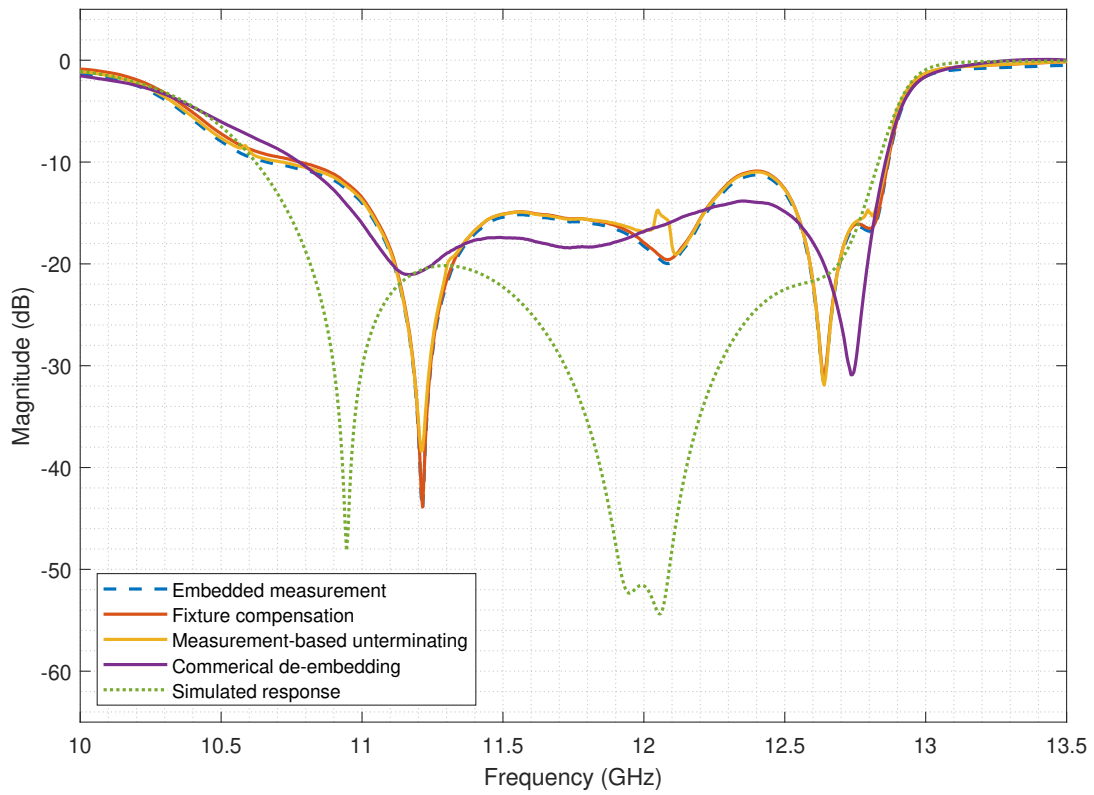


(b) Return loss S_{11}

Figure 7.7: Comparison of manual TRL unterminating & de-embedding methods



(a) Injecton loss S_{21}



(b) Return loss S_{11}

Figure 7.8: Comparison of ECal unterminating & de-embedding methods

7.3 Diplexer

A diplexer is a three-port device with two distinct non-contiguous passbands. The terms diplexer and duplexer are often used interchangeably, even though this is not strictly true [47]. Nevertheless, the studied component will be referred to as *diplexer* hereafter, although it might instead be classified as a duplexer, depending on the specific use case. The crucial characteristics include but are not limited to, the passband insertion loss for both passbands and the isolation between the two passbands. Considered is MW44200 by MinWave, a render is shown in Figure 7.9a, the appropriate port schematic is shown in Figure 7.9b, which is explained in further detail in Table 7.2. The diplexer uses custom waveguide dimensions with custom flanges. Ports COM and RXL share the same waveguide dimensions, whereas TXH features a narrower channel for fundamental-mode operation at higher frequencies.

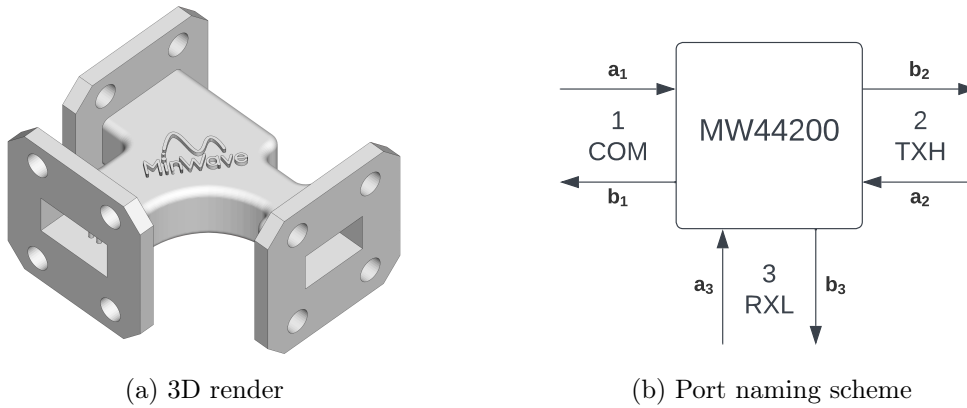


Figure 7.9: MinWave MW44200 diplexer

Port Number	Port Name	Flange	Dimensions
1	COM	COM	10.00 mm · 4.90 mm
2	TXH	TXH	8.64 mm · 4.90 mm
3	RXL	COM	10.00 mm · 4.90 mm

Table 7.2: Diplexer port characteristics

7.3.1 Measurement Plan

The diplexer should be measured and characterised over a frequency range from 15 GHz up to 40 GHz. Covering this large range in the fundamental mode regime for accurate measurement requires the use of different waveguide sizes. Waveguides WR-51, WR-42, WR-34, and WR-28 (cf. Table A.2 for waveguide specifications) have been chosen for this purpose. A schematic overview of how the operative ranges of these waveguides standards overlap is visualised in Figure 7.10. To adapt the custom channel dimensions (COM and TXH) to these four waveguide standards, tapers had to be designed with the methodology presented in section 3.2. As two tapers are required for the 2x-thru measurement needed for de-embedding, a total of 16 tapers had to be manufactured, shown in Figure 7.11, including two COM-TXH tapers for validation. Full measurement of the diplexer requires

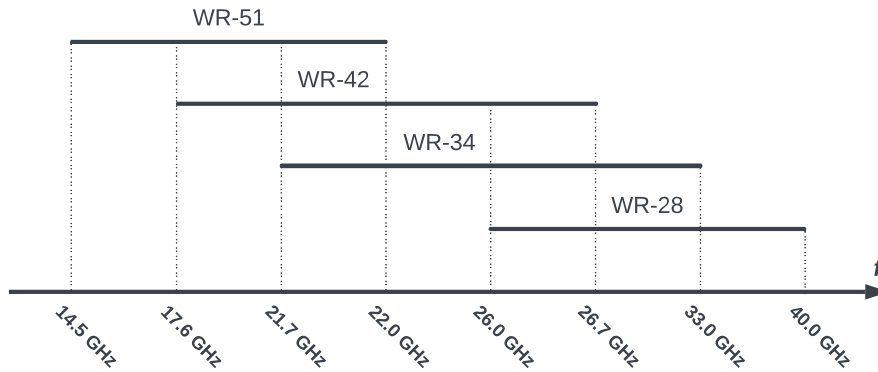


Figure 7.10: Waveguide operating frequency ranges, data based on [46]

$4 \cdot (3 + 2) = 20$ individual two-port measurements: for each of the four relevant waveguide standards, three two-port measurements with the third port terminated, in addition to two 2x-thru measurements to characterise the tapers. The 2x-thru and bisected measurements of the tapers are shown in Figure B.4 and Figure B.5 within Appendix B. For illustrative purposes, some photos of the measurement setup are shown in Figure 7.13. Specifically, the steps for the measurement are as follows:

- i) Measure the diplexer with each of the four relevant waveguide standards (i.e. WR-51/43/34/28) on the complete respective operating frequency range.
- ii) For each waveguide standard, perform three measurements for two ports at once, with the third port terminated with a short or open termination.
- iii) For each of these measurements, acquire data calibrated through manual TRL and ECal.
- iv) In addition to the diplexer itself, measure each pair of used tapers for subsequent de-embedding.

7.3.2 Fabrication & Machining

7.3.2.1 Waveguide Tapers

As mentioned in subsection 7.3.1, waveguide tapers had to be designed for the measurements of the diplexer. These tapers were manufactured through *Craftcloud*¹ using a Selective Laser Melting (SLM) process in aluminium alloy AlSi₁₀Mg [48]. SLM leads to a rather rough surface finish; therefore, the components are sandblasted after production. This process allows for a layer height of 0.15 mm with an accuracy of $\pm 0.2\%$ (with a lower limit of ± 0.2 mm) [49]. Returning to the discussion in subsection 3.2.3 regarding the taper profile, any highly optimised profile on such small waveguides is indeed constrained by the manufacturing process in the case of SLM.

The surface finish obtained through sandblasting may be sufficient for the interior walls of the waveguide taper; however, the flanges need to be machined further to allow for a highly parallel surface profile with low roughness. This was accomplished by machining the flanges with a face milling tool at the Student Prototyping and Outreach Tank (SPOT) at EPFL; this process is visualised in Figure 7.12.

¹Craftcloud[®] by A113DP | 3D Printing Service Marketplace (<https://craftcloud3d.com/>)

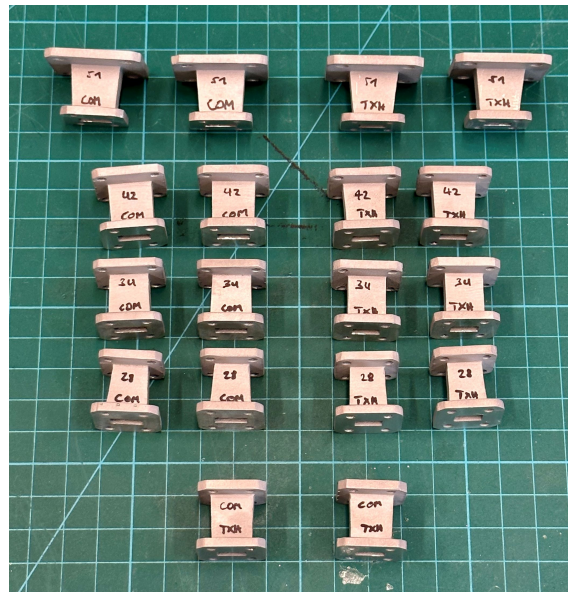


Figure 7.11: Manufactured tapers for port adaptation and validation

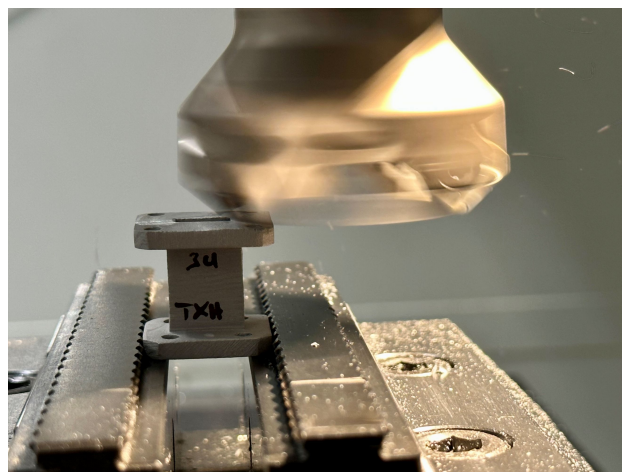
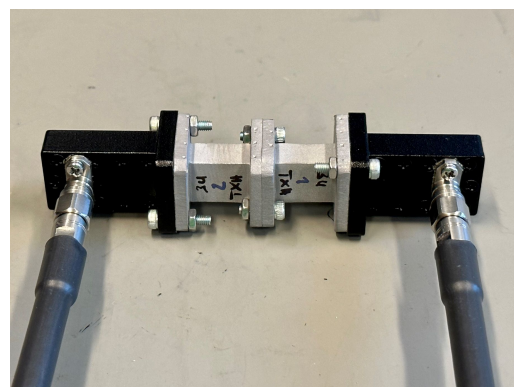


Figure 7.12: Face milling of waveguide tapers



(a) WR-51 RXL – COM measurement



(b) WR-51 – COM taper 2x-thru measurement

Figure 7.13: Diplexer measurement setups

7.3.2.2 TRL Calibration Kit

Appropriate calibration kits had to be used for the manual TRL calibrations of the waveguide standards employed for the measurements. The required shorts and shims were available for WR-75 (used for the double-ridged waveguides in section 7.2), WR-42, WR-34, and WR-28. However, no calibration standards were at hand for WR-51. Therefore, a short and a shim had to be machined with appropriate channel dimensions and flanges as shown in Table A.2. The length of the $\lambda/4$ shim was computed by taking the geometric mean of the lower and upper frequency bounds of the waveguide as shown in Equation 7.1. Indeed, the Figure 5.3 shown earlier in chapter 5 illustrates the shim and short machined at the Student Prototyping and Outreach Tank (SPOT) at EPFL.

$$l = \frac{\lambda}{4} = \frac{c}{4f} = \frac{c}{4\sqrt{f_1 f_2}} = \frac{299.6953 \cdot 10^8 \text{ m/s}}{4\sqrt{14.5 \text{ GHz} \cdot 22.0 \text{ GHz}}} \approx 4.2 \text{ mm} \quad (7.1)$$

7.3.3 Data Fusion

The following sections explain how a three-port measurement is obtained from the 20 individual two-port measurements across multiple waveguide standards for the whole frequency range.

7.3.3.1 Port Augmentation

The wave identification method in subsection 6.4.2 presents a solid framework for combining three two-port measurements into a single three-port measurement, independent of the used terminations. However, this method could not be fully used for its intended purpose due to circumstances explained in further detail in section 8.4. If wave augmentation is performed on a set of measurements where the reflective terms (i.e. S_{11} , S_{22} , S_{33}) differ significantly where they should rather coincide, ambiguities may arise in the final result. As the diplexer represents a particular case of a three-port device, the three-port S -parameter matrix may be assembled directly using Equation 6.7 by identifying the physically relevant reflective terms for a given passband.

7.3.3.2 Frequency Fusion

Coming back to Figure 7.10, most sections of the relevant frequency range from 14.5 GHz to 40.0 GHz are covered by two or even three waveguide standards simultaneously. To make use of this data without unnecessarily truncating it, the concerned final spectrum is obtained by applying the geometric mean on the magnitude values in dB, as shown in Equation 7.2, with k the index to iterate over the n waveguide standards which overlap for a given part of the spectrum. The full spectrum can be merged using the MATLAB implementation shown in Listing C.5.

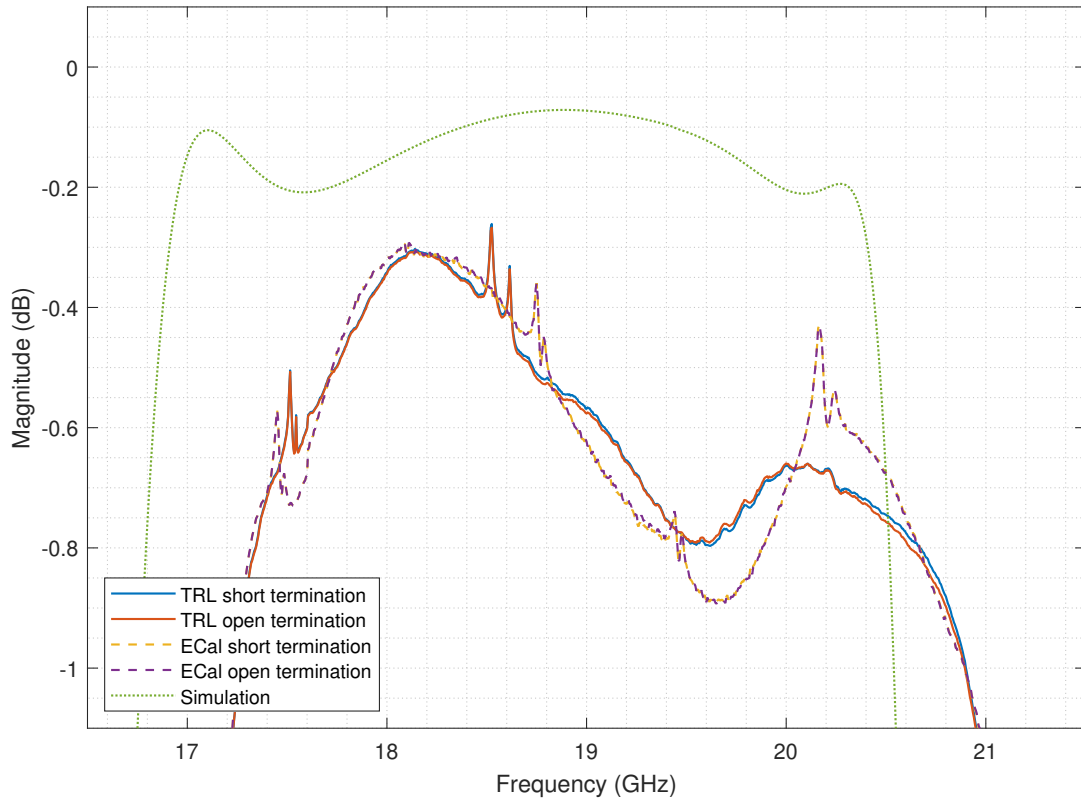
$$S_{ij}' [\text{dB}] = \left(\prod_{k=1}^n S_{ij,k} [\text{dB}] \right)^{1/n} \quad i, j = 1, 2, 3 \quad (7.2)$$

7.3.4 Method Comparison

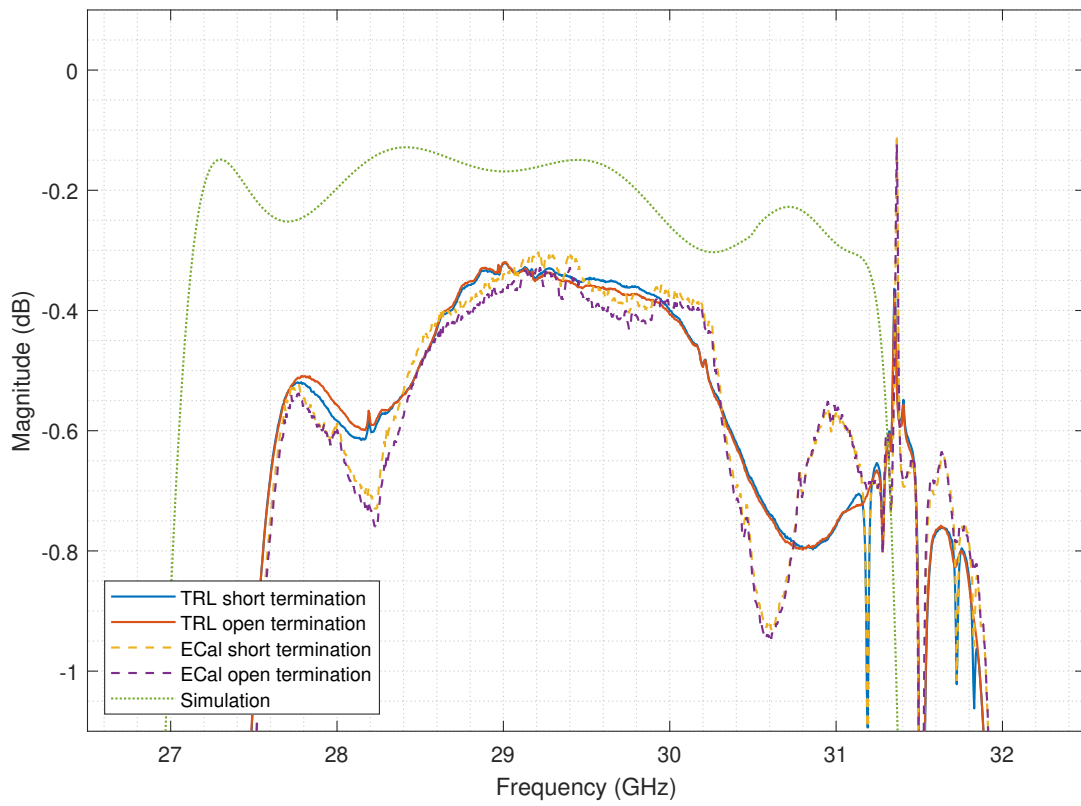
Different calibration methods and terminations can be compared once a final three-port measurement has been assembled for the full frequency range. Considered are the effects of terminating the third port in a short or open circuit, in addition to performing a manual TRL or ECal calibration at different reference planes, as explained earlier. Of particular interest is the insertion loss for the two passbands of the diplexer; the lower passband (between ports COM and RXL) and the upper passband (between ports COM and TXH)

are shown in Figure 7.14a and Figure 7.14b, respectively. Figure 7.15 displays the return loss observed from the COM port. The spectra of the total nine terms of the S -parameter matrix for the four methods are shown in Figure B.6 within Appendix B. The simulation results are shown in Figure 7.16 for comparison.

A frequency shift of about 0.5 GHz can be observed between the measurements and the results expected from the simulation. This effect arises due to shrinkage in the fabrication process of the characterised diplexer. Nonetheless, the measurements cluster tightly together, independent of the chosen method, although some additional loss is incurred. This allows for two essential observations: firstly, there is virtually no difference between the short and open terminations within the passband; secondly, the manual TRL and ECal measurements match closely, indicating that calibrating the setup at the coax lines may indeed be sufficient for such a case.



(a) Lower passband injection loss S_{31}



(b) Upper pass band injection loss S_{21}

Figure 7.14: Comparison of passbands for different methods

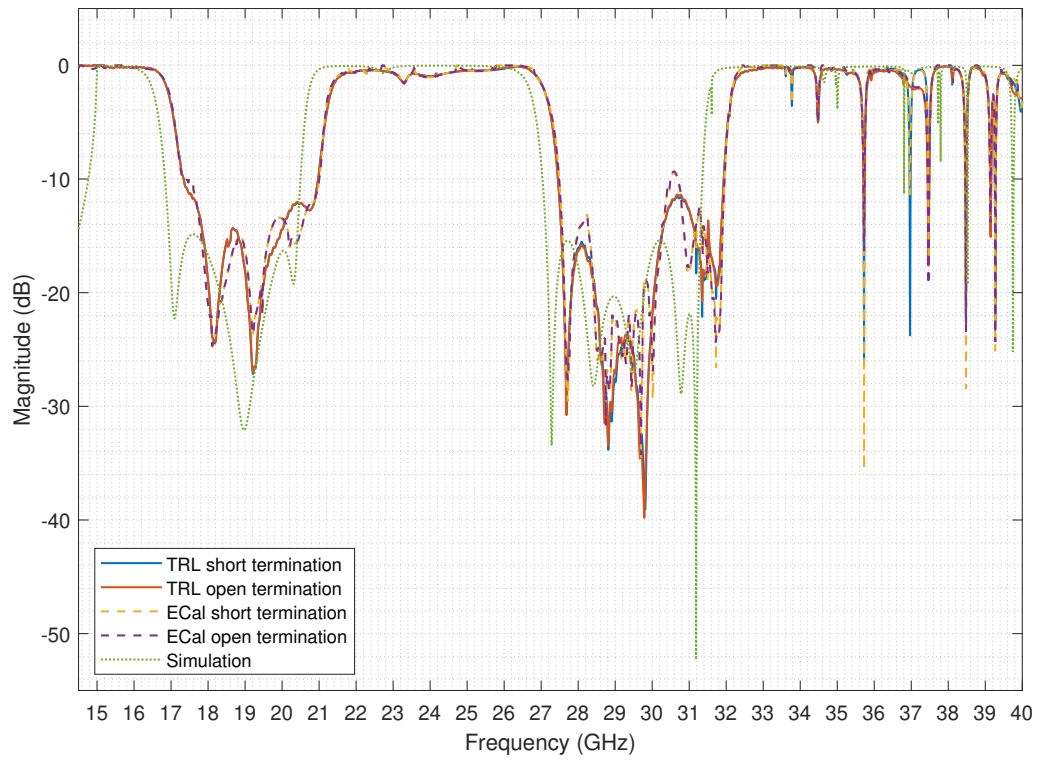


Figure 7.15: Comparison of S_{11} across full spectrum for different methods

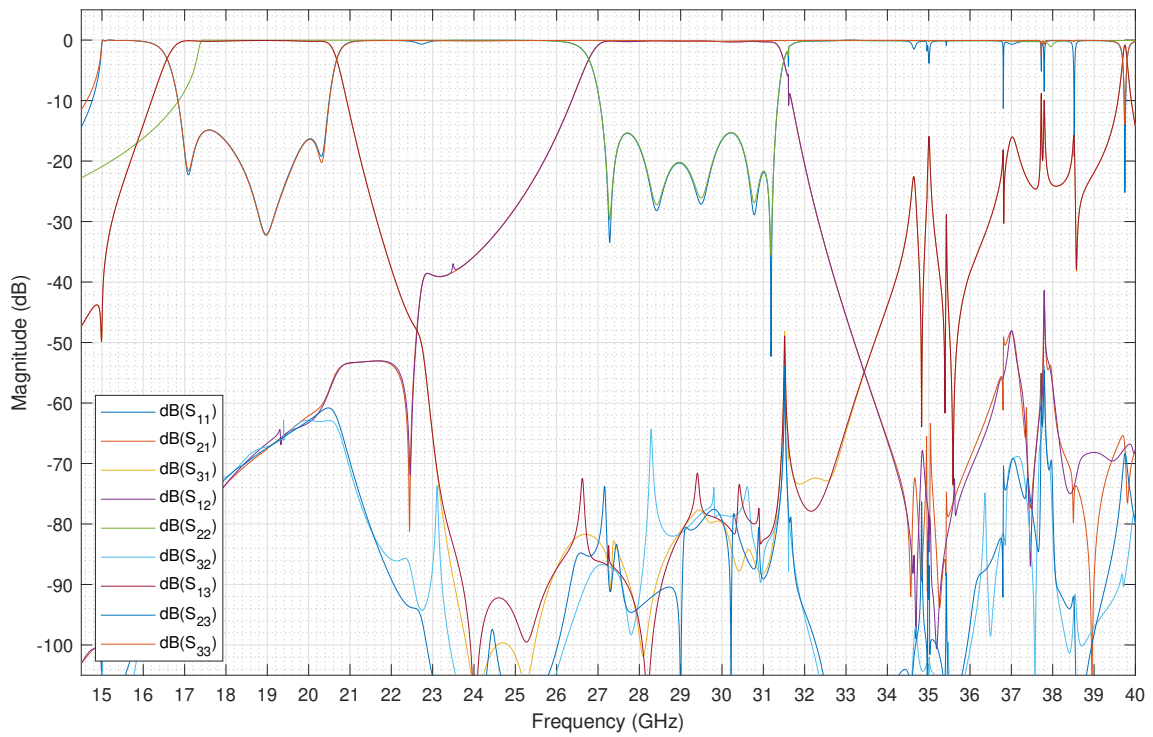


Figure 7.16: MW44200 simulated magnitude S -parameters

Discussion

The following sections extend the preliminary conclusions of chapter 7 by contrasting them with the theoretical foundations presented earlier.

8.1 Bisection Methods

As presented in section 6.2 and subsection 7.2.2, the matrix square roots required in the bisection step can be computed using different methods. To some extent, the main issue influencing all presented techniques is that the square root of a complex number is not uniquely defined [50]. Standard algorithms, however, only yield one result, causing singularities in the presented data when a sign reversal occurs for the real/complex part of the underlying S -parameter value. This behaviour becomes especially noticeable for the Schur decomposition and the input parasitics techniques, as may be observed, for example, in Figure 7.6a and Figure 7.6b. In the implementation of the eigenvalue decomposition (cf. subsection 6.2.1), the input S -parameters are forced into the first quadrant of the complex plane, by taking the absolute values of both the real and imaginary part, before applying the square root. In most cases, this workaround avoids the problem, although some discontinuities may still occur (e.g. bisected measurement of WR-51 – TXH taper shown in Figure B.5). Furthermore, this approach renders the phase data of the measured S -parameters unusable, and an alternative solution has to be identified if the phase behaviour of the DUT is of interest.

8.2 Unterminating & De-Embedding Conclusions

Returning to the preliminary comparison between the different unterminating and de-embedding options presented in Table 7.1 and the preliminary conclusions subsection 7.2.3, some main points should be reiterated. First of all, ECal calibration with the reference plane on the coaxial connectors is a viable method if no waveguide TRL calibration kit is available, although the measurement accuracy is decreased compared with calibration on the waveguide flanges as reference planes. Measurement-based unterminating with bisection performed via the matrix diagonalisation method (cf. subsection 6.2.1) delivers the results closest to simulated and commercial solutions. However, the overall discussion only applies to the magnitude of the processed S -parameters, to which extent accurate phase measurements can be obtained has to be validated in further experiments.

8.3 Passivity

Any algorithm applied to S -parameter data (e.g. bisection, de-embedding, port augmentation) may cause issues with the passivity of the measurement (cf. subsection 4.2.1). For example, Figure 8.1a shows the passivity plot of the diplexer for the TRL measurement with open termination and Figure 8.1b the passivity plot of the simulated S -parameters. Passivity can be enforced in MATLAB using the `makepassive` function [51]. Figure B.7 in

Appendix B presents the diplexer measurement results if passivity is enforced, mainly leading to increased insertion loss. Whether this represents an issue within the post-processing of the measurements or is due to purely mathematical artefacts (especially as it also applies to simulated S -parameters) is a topic for further investigation.

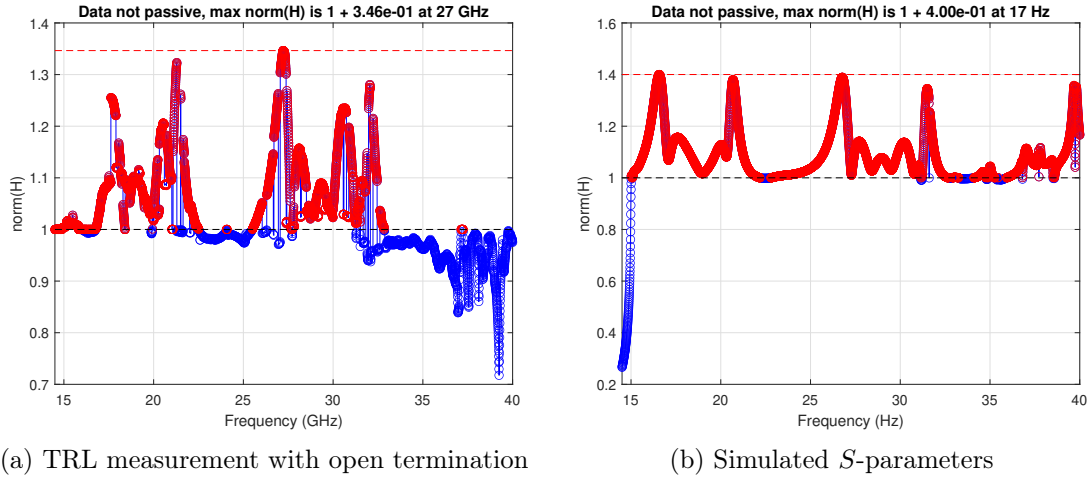


Figure 8.1: Diplexer passivity plots

8.4 Port Augmentation

In section 8.4, combining two-port measurements to obtain a three-port measurement was presented in the context of the diplexer measurements. As mentioned, the wave identification method [44] could not be fully used for its intended purpose. The diplexer represents a particular case of a three-port device, as the TXH and RXL ports are isolated from each other. This becomes clearly visible by comparing the responses for open and short terminations, with no significant difference arising in the insertion loss. Therefore, applying a port augmentation method like wave identification will necessarily lead to numerical issues, as it expects contributions on all three ports for all frequencies. Performing wave identification with $\Gamma = -0.8$ as an approximation of a short circuit on the short-terminated measurements leads to the results shown in Figure 8.2. Peaks with magnitude > 0 dB are observable, which indicate an issue in the algorithm, as the passive diplexer cannot produce any gain.

In the case of the diplexer, the S -parameters of the individual two-port measurements may be merged manually as shown in Equation 6.7. Prior knowledge about the expected behaviour is used to identify the origin of the physically accurate reflection terms S_{11} , S_{22} , and S_{33} for the specific passband, in each case choosing the isolated terms for the non-contributing port.

8.5 Characteristic Impedances

As introduced in subsection 3.1.3, the characteristic impedance of a waveguide device is not constant but a function of the frequency. When only dealing with physical measurements obtained through the VNA, this does not directly pose a problem, as the VNA always sees the 50Ω input impedance of the test assembly, due to the coax-to-waveguide adapters. However, the situation becomes more intricate when dealing with simulation results. Any S -parameters obtained through simulation will be normalised with respect to the waveguide port impedance. This means that different normalisations per port will apply for simulation

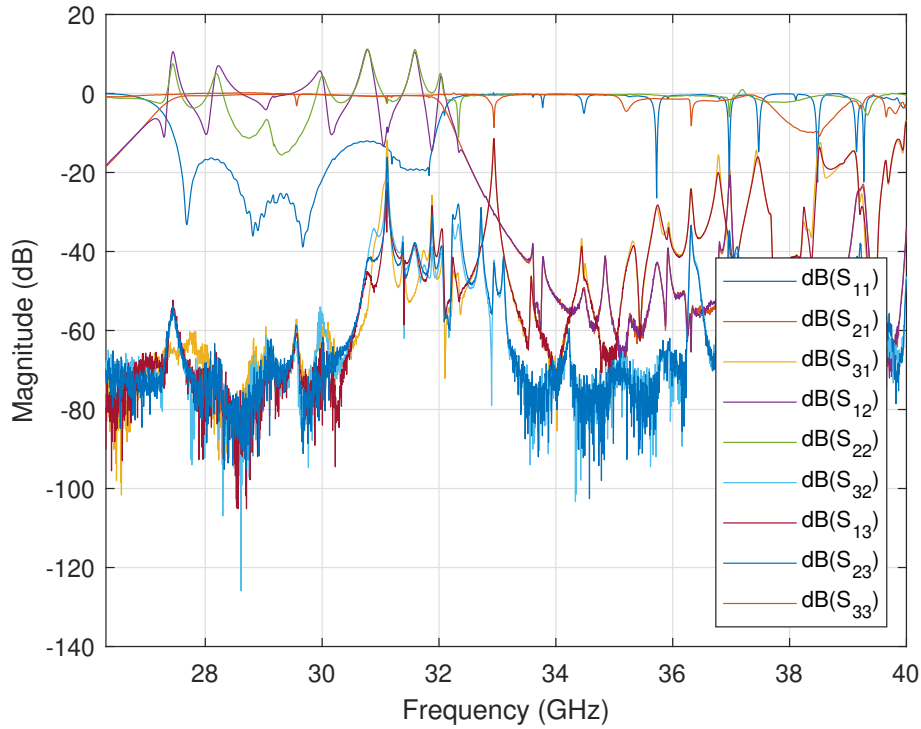


Figure 8.2: Result of wave identification with $\Gamma = -0.8$ on WR-28 short measurement

results of asymmetric devices (e.g. waveguide tapers) where the characteristic impedance profile is not the same on both ports. Therefore, special care must be taken to obtain the expected behaviour when simulation results are merged with measurement results (cf. simulation-based unterminating subsection 7.2.3); the same applies when constructing a cascade of simulated components with different impedance profiles. When converting from S to $ABCD$ -parameters, as well as for the inverse operation, it is essential to specify the appropriate characteristic impedance. If the source and load impedances are the same for a given device, the parameter conversion formulas in subsection A.3.2.1 within Appendix A apply. If the source and load impedances are not the same, as is the case for waveguide tapers, the conversions in subsection A.3.2.2 may be used.

Conclusion

This project focused on studying and establishing measurement techniques to characterise the behaviour of waveguide devices, specifically filters and diplexers. The complexity of the problem arose from the unique properties of the Devices Under Test (DUTs), requiring particular methods to validate the components' measurements accurately. The measurements conducted throughout this project were performed on waveguide devices developed by MinWave, a company specialising in the design of non-conventional waveguide devices using additive manufacturing methods.

In general, measurements were acquired using different calibration techniques, comparing their advantages and disadvantages. The measurements and analyses of the double-ridged waveguide filters demonstrate the effectiveness of the developed unterminating and de-embedding techniques. Different methods of obtaining the bisected fixture behaviour via a 2x-thru measurement were studied. Additionally, various de-embedding methods were compared, including measurement-based techniques, simulation-aided approaches, and commercial solutions.

The diplexer measurements involved a comprehensive measurement plan, considering different waveguide sizes to accurately cover the desired frequency range. Custom tapers were designed and fabricated to interface the custom waveguide dimensions with the chosen waveguide standards. The measurement setup included multiple two-port measurements for each waveguide standard, with the third port terminated, as well as 2x-thru measurements for taper characterisation. The acquired data was fused to obtain a three-port measurement for the whole frequency range.

Overall, the development of this project proved to be an exciting combination of subjects, requiring developments and analyses in electrical engineering, mechanical engineering, software development, and mathematics.

List of Figures

3.1	Rectangular waveguide illustrations, reproduced from [1, p. 131, 138]	6
3.2	Waveguide fundamental mode impedance with $f_c = 10$ GHz	8
3.3	Linear waveguide taper VSWR transitioning from COM to WR-28	9
4.1	Light-wave scattering analogy, reproduced from [6]	10
4.2	Transmission line terminated in load impedance Z_L , reproduced from [1, p. 57]	10
4.3	S -parameter measurement, reproduced from [6]	12
4.4	$ABCD$ representation, reproduced from [1]	12
5.1	One-port error model signal flow graph, reproduced from [12]	13
5.2	Two-port forward error model signal flow graph, reproduced from [12]	14
5.3	WR-51 manual TRL calibration kit including shim and short	15
6.1	Signal flow graph of the test fixtures and DUT, reproduced from [12]	17
6.2	Signal flow graph of the combined test setup with forward error terms, reproduced from [12]	18
6.3	2x-thru measurement equivalent circuit model, reproduced from [26]	19
7.1	Double-ridged waveguide components	24
7.2	Schematic measurement setups of the embedded DUT	25
7.3	Photos of the filter measurement setups represented in Figure 7.2	25
7.4	MW13200 embedded magnitude S -parameter measurements	26
7.5	MW13200 simulated magnitude S -parameters	26
7.6	Comparison of manual TRL bisection methods	27
7.7	Comparison of manual TRL unterminating & de-embedding methods	29
7.8	Comparison of ECal unterminating & de-embedding methods	30
7.9	MinWave MW44200 diplexer	31
7.10	Waveguide operating frequency ranges	32
7.11	Manufactured tapers for port adaptation and validation	33
7.12	Face milling of waveguide tapers	33
7.13	Diplexer measurement setups	33
7.14	Comparison of passbands for different methods	36
7.15	Comparison of S_{11} across full spectrum for different methods	37
7.16	MW44200 simulated magnitude S -parameters	37
8.1	Diplexer passivity plots	39
8.2	Result of wave identification with $\Gamma = -0.8$ on WR-28 short measurement	40
B.1	MW13200 de-embedded S -parameters method comparison	53
B.2	MW13200 de-embedded S -parameters for simulation-based unterminating	53
B.3	MW13200 de-embedded S -parameters unterminating comparison	54
B.4	2x-thru and bisected measurements of COM tapers	55
B.5	2x-thru and bisected measurements of TXH tapers	56
B.6	Diplexer measurement method comparison	57
B.7	Passivated diplexer measurement method comparison	58

List of Tables

5.1	Comparison of manual TRL and ECal calibration methods	15
7.1	Unterminating/de-embedding method comparison	28
7.2	Diplexer port characteristics	31
A.1	IEEE radar-frequency letter band nomenclature with ITU nomenclature [52]	50
A.2	Specifications of standard and custom waveguides [46], [53]	50

Acronyms

AITT	Advanced Interconnect Test Tool
DUT	Device Under Test
ECal	Electronic Calibration
EHF	Extremely High Frequency
EZD	EaZy De-Embedding
IEEE	Institute of Electrical and Electronics Engineers
ISD	In-Situ De-Embedding
ITU	International Telecommunication Union
LWE	Laboratory of Wave Engineering
MAG	Microwave and Antenna Group
MIAOU	Microwave Input And Output Unit
PCB	Printed Circuit Board
RF	Radiofrequency
SHF	Super High Frequency
SLM	Selective Laser Melting
SOL	Short – Open – Load
SOLT	Short – Open – Load – Through
SPOT	Student Prototyping and Outreach Tank
TE	Transverse Electric
TOM	Through – Open – Match
TOSM	Through – Open – Short – Match
TRL	Through – Reflect – Line
TRM	Through – Reflect – Match
TSM	Through – Short – Match
UHF	Ultra High Frequency
UOSM	Unknown Through – Open – Short – Match
VNA	Vector Network Analyser
VSWR	Voltage Standing Wave Ratio
WG	Waveguide

Bibliography

- [1] D. M. Pozar, *Microwave Engineering*, 4th Edition. John Wiley & Sons, Inc., Nov. 2011, ISBN: 978-0-470-63155-3.
- [2] J. D. Jackson, *Classical Electrodynamics*, 3rd ed. John Wiley & Sons, Inc., 1999, ISBN: 0-471-30932-X.
- [3] J. A. Seeger, *Microwave Theory, Components, and Devices*. Prentice-Hall, 1986, ISBN: 0-13-581612-2.
- [4] R. Johnson, "Design of Linear Double Tapers in Rectangular Waveguides," *IRE Transactions on Microwave Theory and Techniques*, vol. 7, no. 3, Jul. 1959, Conference Name: IRE Transactions on Microwave Theory and Techniques, ISSN: 2331-088X. DOI: 10.1109/TMTT.1959.1124594.
- [5] R. W. Klopfenstein, "A Transmission Line Taper of Improved Design," *Proceedings of the IRE*, vol. 44, no. 1, Jan. 1956, Conference Name: Proceedings of the IRE, ISSN: 2162-6634. DOI: 10.1109/JRPROC.1956.274847.
- [6] Keysight Technologies, *Understanding the Fundamental Principles of Vector Network Analysis*, Application Note, Aug. 2022. [Online]. Available: <https://www.keysight.com/us/en/assets/7018-06841/application-notes/5965-7707.pdf>.
- [7] V. Teppati, A. Ferrero and M. Sayed, Eds., *Modern RF and Microwave Measurement Techniques* (The Cambridge RF and Microwave Engineering Series). Cambridge: Cambridge University Press, 2013, ISBN: 978-1-107-03641-3. DOI: 10.1017/CB09781139567626. (visited on 12/02/2023).
- [8] D. Williams, "Traveling Waves and Power Waves: Building a Solid Foundation for Microwave Circuit Theory," *IEEE Microwave Magazine*, vol. 14, no. 7, Nov. 2013, Conference Name: IEEE Microwave Magazine, ISSN: 1557-9581. DOI: 10.1109/MMM.2013.2279494.
- [9] F. E. Gardiol, *Introduction to Microwaves*. Artech House, 1984, ISBN: 0-89006-134-3.
- [10] D. Frickey, "Conversions between S, Z, Y, H, ABCD, and T parameters which are valid for complex source and load impedances," *IEEE Transactions on Microwave Theory and Techniques*, vol. 42, no. 2, Feb. 1994, Conference Name: IEEE Transactions on Microwave Theory and Techniques, ISSN: 1557-9670. DOI: 10.1109/22.275248.
- [11] F. Caspers, "RF engineering basic concepts: S-parameters," 2011, _eprint: 1201.2346. DOI: 10.5170/CERN-2011-007.67. [Online]. Available: <https://cds.cern.ch/record/1415639> (visited on 12/06/2023).
- [12] Keysight Technologies, *De-Embedding and Embedding S-Parameter Networks Using a Vector Network Analyzer*, Application Note, Jul. 2020. [Online]. Available: <https://www.keysight.com/us/en/assets/7018-06806/application-notes/5980-2784.pdf>.
- [13] Keysight Technologies, *Applying Error Correction to Vector Network Analyzer Measurements*, Application Note, Aug. 2022. [Online]. Available: <https://www.keysight.com/us/en/assets/7018-06761/application-notes/5965-7709.pdf>.

- [14] Rohde & Schwarz GmbH & Co. KG, *R&S ZNA User Manual*, 1178.6462.02, Mar. 2023. [Online]. Available: https://scdn.rohde-schwarz.com/ur/pws/dl_downloads/pdm/cl_manuals/user_manual/1178_6462_01/ZNA_UserManual_en_30.pdf (visited on 18/06/2023).
- [15] Keysight Technologies, *Operating and Service Manual 11644A R, Q, U, V, and W Waveguide Calibration Kits*, May 2022. [Online]. Available: <https://www.keysight.com/us/en/assets/9018-01042/user-manuals/9018-01042.pdf?success=true> (visited on 20/06/2023).
- [16] R. Soares, P. Gouzien, P. Legaud and G. Follot, "A unified mathematical approach to two-port calibration techniques and some applications," *IEEE Transactions on Microwave Theory and Techniques*, vol. 37, no. 11, Nov. 1989, Conference Name: IEEE Transactions on Microwave Theory and Techniques, ISSN: 1557-9670. DOI: 10.1109/22.41029.
- [17] J. Juroshek, C. Hoer and R. Kaiser, "Calibrating network analyzers with imperfect test ports," *IEEE Transactions on Instrumentation and Measurement*, vol. 38, no. 4, Aug. 1989, Conference Name: IEEE Transactions on Instrumentation and Measurement, ISSN: 1557-9662. DOI: 10.1109/19.31010.
- [18] D. K. Rytting, "Network Analyzer Accuracy Overview," in *58th ARFTG Conference Digest*, vol. 40, Nov. 2001. DOI: 10.1109/ARFTG.2001.327486.
- [19] D. F. Williams, "Rectangular-waveguide vector-network-analyzer calibrations with imperfect test ports," in *2010 76th ARFTG Microwave Measurement Conference*, Nov. 2010. DOI: 10.1109/ARFTG76.2010.5700048.
- [20] A. R. Kerr, *Mismatch Caused by Waveguide Tolerances, Corner Radii, and Flange Misalignment*, Electronics Division Technical Note No. 215, Dec. 2009. [Online]. Available: <https://www.gb.nrao.edu/electronics/edtn/edtn215.pdf>.
- [21] R. Bauer and P. Penfield, "De-Embedding and Unterminating," *IEEE Transactions on Microwave Theory and Techniques*, vol. 22, no. 3, Mar. 1974, Conference Name: IEEE Transactions on Microwave Theory and Techniques, ISSN: 1557-9670. DOI: 10.1109/TMTT.1974.1128212.
- [22] H. Barnes and J. Moreira, "Verifying the accuracy of 2x-Thru de-embedding for un-symmetrical test fixtures," in *2017 IEEE 26th Conference on Electrical Performance of Electronic Packaging and Systems (EPEPS)*, ISSN: 2165-4115, Oct. 2017. DOI: 10.1109/EPEPS.2017.8329760.
- [23] B. W. Levinger, "The Square Root of a 2×2 Matrix," *Mathematics Magazine*, vol. 53, no. 4, 1980, Publisher: Mathematical Association of America, ISSN: 0025-570X. DOI: 10.2307/2689616. [Online]. Available: <https://www.jstor.org/stable/2689616> (visited on 12/06/2023).
- [24] E. Deadman, N. J. Higham and R. Ralha, "Blocked Schur Algorithms for Computing the Matrix Square Root," in *Applied Parallel and Scientific Computing*, P. Manninen and P. Öster, Eds., ser. Lecture Notes in Computer Science, Berlin, Heidelberg: Springer, 2013, ISBN: 978-3-642-36803-5. DOI: 10.1007/978-3-642-36803-5_12.
- [25] MathWorks, *Bisect S-Parameters of Cascaded Probes - MATLAB & Simulink*. [Online]. Available: <https://ch.mathworks.com/help/rf/ug/bisecting-s-parameters-of-cascaded-probes.html> (visited on 12/06/2023).

- [26] S. Simion, "A New Unterminating Method for De-Embedding the Coaxial to Waveguide Transitions," *Progress In Electromagnetics Research C*, vol. 121, 2022, ISSN: 1937-8718. DOI: 10.2528/PIERC22053105. [Online]. Available: <http://www.jpier.org/PIERC/pier.php?paper=22053105> (visited on 06/03/2023).
- [27] S. Simion, "A Simple Method for De-embedding the Coaxial to Waveguide Transitions," in *2022 International Semiconductor Conference (CAS)*, ISSN: 2377-0678, Oct. 2022. DOI: 10.1109/CAS56377.2022.9934624.
- [28] R. d. Azevedo, *How to solve $A^{1/2} B A^{1/2} = C$ for A ?* Published: Mathematics Stack Exchange. [Online]. Available: <https://math.stackexchange.com/q/3141200>.
- [29] Keysight Technologies, *Time Domain Analysis Using a Network Analyzer*, Application Note, Jun. 2020. [Online]. Available: <https://www.keysight.com/us/en/assets/7018-01451/application-notes/5989-5723.pdf>.
- [30] L. Van Hauwermeiren, M. Botte and D. De Zutter, "A new de-embedding technique for on-board structures applied to the bandwidth measurement of packages," *IEEE Transactions on Components, Hybrids, and Manufacturing Technology*, vol. 16, no. 3, May 1993, Conference Name: IEEE Transactions on Components, Hybrids, and Manufacturing Technology, ISSN: 1558-3082. DOI: 10.1109/33.232056.
- [31] J. Dunsmore, N. Cheng and Y.-x. Zhang, "Characterizations of asymmetric fixtures with a two-gate approach," in *77th ARFTG Microwave Measurement Conference*, Jun. 2011. DOI: 10.1109/ARFTG77.2011.6034555.
- [32] A. Chakraborty and G. Sanyal, "Transmission Matrix of a Linear Double Taper in Rectangular Waveguides," *IEEE Transactions on Microwave Theory and Techniques*, vol. 28, no. 6, Jun. 1980, Conference Name: IEEE Transactions on Microwave Theory and Techniques, ISSN: 1557-9670. DOI: 10.1109/TMTT.1980.1130122.
- [33] R. Shaver, "Analysis of the Tapered Transition Waveguide," *Browse all Theses and Dissertations*, Jan. 2015. [Online]. Available: https://corescholar.libraries.wright.edu/etd_all/1285.
- [34] Keysight Technologies, *Signal Integrity Analysis Series Part 3: De-Embedding*, Application Note, Jul. 2014. [Online]. Available: <https://www.keysight.com/us/en/assets/7018-08491/application-notes/5989-5765.pdf>.
- [35] S. Scafati, F. de Paulis, C. Olivieri and A. Orlandi, "Generalized analytical formulation for de-embedding of multiport devices based on known fixtures," *International Journal of RF and Microwave Computer-Aided Engineering*, vol. 32, no. 11, 2022, ISSN: 1099-047X. DOI: 10.1002/mmce.23336. [Online]. Available: <https://onlinelibrary.wiley.com/doi/abs/10.1002/mmce.23336> (visited on 06/03/2023).
- [36] W. Wang, R. Jin, T. S. Bird, X. Liang and J. Geng, "De-Embedding Based on EM Simulation and Measurement: A Hybrid Method," *IEEE Transactions on Microwave Theory and Techniques*, vol. 65, no. 12, Dec. 2017, Conference Name: IEEE Transactions on Microwave Theory and Techniques, ISSN: 1557-9670. DOI: 10.1109/TMTT.2017.2715326.
- [37] *IEEE Standard for Electrical Characterization of Printed Circuit Board and Related Interconnects at Frequencies up to 50 GHz*, IEEE Std 370™-2020, Jan. 2021. DOI: 10.1109/IEEESTD.2021.9316329.

- [38] J. Ellison, S. B. Smith and S. Agili, "Using a 2x-thru standard to achieve accurate de-embedding of measurements," *Microwave and Optical Technology Letters*, vol. 62, no. 2, 2020, ISSN: 1098-2760. DOI: 10.1002/mop.32098. [Online]. Available: <https://onlinelibrary.wiley.com/doi/abs/10.1002/mop.32098> (visited on 06/03/2023).
- [39] J. Ellison and S. Agili, "Impedance Corrected De-Embedding," *IEEE Electromagnetic Compatibility Magazine*, vol. 11, no. 3, 2022, Conference Name: IEEE Electromagnetic Compatibility Magazine, ISSN: 2162-2272. DOI: 10.1109/MEMC.2022.9982534.
- [40] J. Ellison and J. Gay, *GitLab IEEE 370*, Feb. 2023. [Online]. Available: <https://opensource.ieee.org/elec-char/ieee-370> (visited on 06/03/2023).
- [41] Clear Signal Solutions, *Advanced Interconnect Test Tool (AITT)*. [Online]. Available: <https://clearsig.com/clearsig/> (visited on 08/03/2023).
- [42] AtaiTec, *In-Situ De-embedding (ISD)*. [Online]. Available: <https://ataitec.com/products/isd/> (visited on 18/06/2023).
- [43] J. Tippet and R. Speciale, "A Rigorous Technique for Measuring the Scattering Matrix of a Multiport Device with a 2-Port Network Analyzer," *IEEE Transactions on Microwave Theory and Techniques*, vol. 30, no. 5, May 1982, ISSN: 0018-9480. DOI: 10.1109/TMTT.1982.1131118. [Online]. Available: <http://ieeexplore.ieee.org/document/1131118/> (visited on 10/05/2023).
- [44] I. Rolfes and B. Schiek, "Multiport method for the measurement of the scattering parameters of N-ports," *IEEE Transactions on Microwave Theory and Techniques*, vol. 53, no. 6, Jun. 2005, Conference Name: IEEE Transactions on Microwave Theory and Techniques, ISSN: 1557-9670. DOI: 10.1109/TMTT.2005.848823.
- [45] B. Will, I. Rolfes and B. Schiek, "Novel algorithms for the characterization of n-port networks by using a two-port network analyzer," *Advances in Radio Science*, vol. 5, no. A.1, Jun. 2007, Conference Name: Kleinheubacher Berichte 2006 - Publisher: Copernicus GmbH, ISSN: 1684-9965. DOI: 10.5194/ars-5-13-2007. [Online]. Available: <https://ars.copernicus.org/articles/5/13/2007/> (visited on 19/05/2023).
- [46] H.-U. Nickel, *Cross Reference for Hollow Metallic Waveguides*, TD-00036, Sep. 2022. [Online]. Available: <https://www.microwaves101.com/uploads/TD-00036S-Ulis-waveguide-list.pdf> (visited on 26/05/2023).
- [47] *Antenna Diplexer: Splitter / Combiner » Electronics Notes*. [Online]. Available: <https://www.electronics-notes.com/articles/antennas-propagation/antenna-diplexer/what-is-antenna-diplexer.php> (visited on 16/06/2023).
- [48] *How to pick the most suitable technology for my design*. [Online]. Available: <https://craftcloud3d.elevio.help/en/articles/27-how-to-pick-the-most-suitable-technology-for-my-design> (visited on 16/06/2023).
- [49] *Design Guide*. [Online]. Available: <https://craftcloud3d.elevio.help/en/articles/32-design-guide> (visited on 16/06/2023).
- [50] E. W. Weisstein, *Square Root - Wolfram MathWorld*, Publisher: Wolfram Research, Inc. [Online]. Available: <https://mathworld.wolfram.com/> (visited on 20/06/2023).
- [51] MathWorks, *Make N-port S-parameters passive - MATLAB makepassive*. [Online]. Available: <https://ch.mathworks.com/help/rf/ref/makepassive.html> (visited on 22/06/2023).

- [52] *IEEE Standard Letter Designations for Radar-Frequency Bands*, IEEE Std 521™-2019, Feb. 2020. DOI: 10.1109/IEEESTD.2020.8999849.
- [53] S. Zauzig and H.-U. Nickel, *Flanges for Ordinary Rectangular Waveguides*, TD-00077, Dec. 2022. [Online]. Available: <https://www.microwaves101.com/uploads/TD-00077L-Simones-flange-list.pdf> (visited on 26/05/2023).

A

Definitions and Conventions

A.1 Radar-Frequency Bands

Radar Nomenclature		ITU Nomenclature	
Band	Frequency Range	Adjectival Band Designation	Metric Designation
L	1 GHz to 2 GHz	Ultra High Frequency (UHF)	Decimetric Waves
S	2 GHz to 4 GHz		
C	4 GHz to 8 GHz	Super High Frequency (SHF)	Centimetric Waves
X	8 GHz to 12 GHz		
K _u	12 GHz to 18 GHz		
K	18 GHz to 27 GHz	Extremely High Frequency (EHF)	Millimetric Waves
K _a	27 GHz to 40 GHz		
V	40 GHz to 75 GHz		
W	75 GHz to 110 GHz		

Table A.1: IEEE radar-frequency letter band nomenclature with ITU nomenclature [52]

A.2 Waveguide Dimensions

Designation	Flange	Inner Dimensions	Cutoff Frequency	Frequency Range
WR-75	UBR 120	19.050 mm · 9.525 mm	7.869 GHz	9.9 GHz to 15.0 GHz
WR-62	UG-419/U	15.799 mm · 7.899 mm	9.488 GHz	11.9 GHz to 18.0 GHz
WR-51	UBR 180	12.954 mm · 6.477 mm	11.571 GHz	14.5 GHz to 22.0 GHz
WR-42	UG-597/U	10.668 mm · 4.318 mm	14.051 GHz	17.6 GHz to 26.7 GHz
WR-34	FBP260	8.636 mm · 4.318 mm	17.357 GHz	21.7 GHz to 33.0 GHz
WR-28	UG-599/U	7.112 mm · 3.556 mm	21.077 GHz	26.3 GHz to 40.0 GHz
	COM	10.000 mm · 4.900 mm	14.990 GHz	–
	TXH	8.640 mm · 4.900 mm	17.349 GHz	–

Table A.2: Specifications of standard and custom waveguides [46], [53]

A.3 Parameter Conversions

A.3.1 T-Parameters

Hereafter follow the parameter conversions from S to T and vice versa [12].

$$\begin{aligned}
T_{11} &= -\frac{S_{11}S_{22} - S_{12}S_{21}}{S_{22}} & S_{11} &= \frac{T_{12}}{T_{22}} \\
T_{12} &= \frac{S_{11}}{S_{21}} & S_{12} &= \frac{T_{11}T_{22} - T_{12}T_{21}}{T_{22}} \\
T_{21} &= -\frac{S_{22}}{S_{21}} & S_{21} &= \frac{1}{T_{22}} \\
T_{22} &= \frac{1}{S_{21}} & S_{22} &= -\frac{T_{21}}{T_{22}}
\end{aligned}$$

A.3.2 ABCD-Parameters

Equations in subsection A.3.2.1 show the conversions between S and $ABCD$ -parameters in the case of a real characteristic line impedance [1, p. 192]. The equations in subsection A.3.2.2 extend these formulations by being applicable to complex impedances; $Z_{01} = R_{01} + jX_{01}$ and $Z_{02} = R_{02} + jX_{02}$ representing the complex source and load impedances, respectively; and Z^* the complex conjugate [10].

A.3.2.1 Real Symmetric Line Impedances

$$\begin{aligned}
A &= \frac{(1 + S_{11})(1 - S_{22}) + S_{12}S_{21}}{2S_{21}} & S_{11} &= \frac{A + B/Z_0 - CZ_0 - D}{A + B/Z_0 + CZ_0 + D} \\
B &= Z_0 \cdot \frac{(1 + S_{11})(1 + S_{22}) - S_{12}S_{21}}{2S_{21}} & S_{12} &= \frac{2(AD - BC)}{A + B/Z_0 + CZ_0 + D} \\
C &= \frac{1}{Z_0} \cdot \frac{(1 - S_{11})(1 - S_{22}) - S_{12}S_{21}}{2S_{21}} & S_{21} &= \frac{2}{A + B/Z_0 + CZ_0 + D} \\
D &= \frac{(1 - S_{11})(1 + S_{22}) + S_{12}S_{21}}{2S_{21}} & S_{22} &= \frac{-A + B/Z_0 - CZ_0 + D}{A + B/Z_0 + CZ_0 + D}
\end{aligned}$$

A.3.2.2 Complex Asymmetric Line Impedances

$$\begin{aligned}
A &= \frac{(Z_{01}^* + S_{11}Z_{01})(1 - S_{22}) + S_{12}S_{21}Z_{01}}{2S_{21}\sqrt{R_{01}R_{02}}} \\
B &= \frac{(Z_{01}^* + S_{11}Z_{01})(Z_{02}^* + S_{22}Z_{02}) - S_{12}S_{21}Z_{01}Z_{02}}{2S_{21}\sqrt{R_{01}R_{02}}} \\
C &= \frac{(1 - S_{11})(1 - S_{22}) - S_{12}S_{21}}{2S_{21}\sqrt{R_{01}R_{02}}} \\
D &= \frac{(1 - S_{11})(Z_{02}^* + S_{22}Z_{02}) - S_{12}S_{21}Z_{02}}{2S_{21}\sqrt{R_{01}R_{02}}} \\
S_{11} &= \frac{AZ_{02} + B - CZ_{01}^*Z_{02} - DZ_{01}^*}{AZ_{02} + B + CZ_{01}Z_{02} + DZ_{01}} \\
S_{12} &= \frac{2(AD - BC)\sqrt{R_{01}R_{02}}}{AZ_{02} + B + CZ_{01}Z_{02} + DZ_{01}} \\
S_{21} &= \frac{2\sqrt{R_{01}R_{02}}}{AZ_{02} + B + CZ_{01}Z_{02} + DZ_{01}} \\
S_{22} &= \frac{-AZ_{02}^* + B - CZ_{01}Z_{02}^* + DZ_{01}^*}{AZ_{02} + B + CZ_{01}Z_{02} + DZ_{01}}
\end{aligned}$$

B

Measurement Results

The plots on the following pages show the measurement data referenced in chapter 7. Each measurement or processing step is represented by two plots of the same data with different scaling on the y -axes, with the plots on the left-hand side displaying the full y -scale, showcasing the behaviour of the return losses (i.e. S_{11} & S_{22}), and the plots on the right-hand side displaying the insertion losses (i.e. S_{21} & S_{12}) within the passband on a more granular scale.

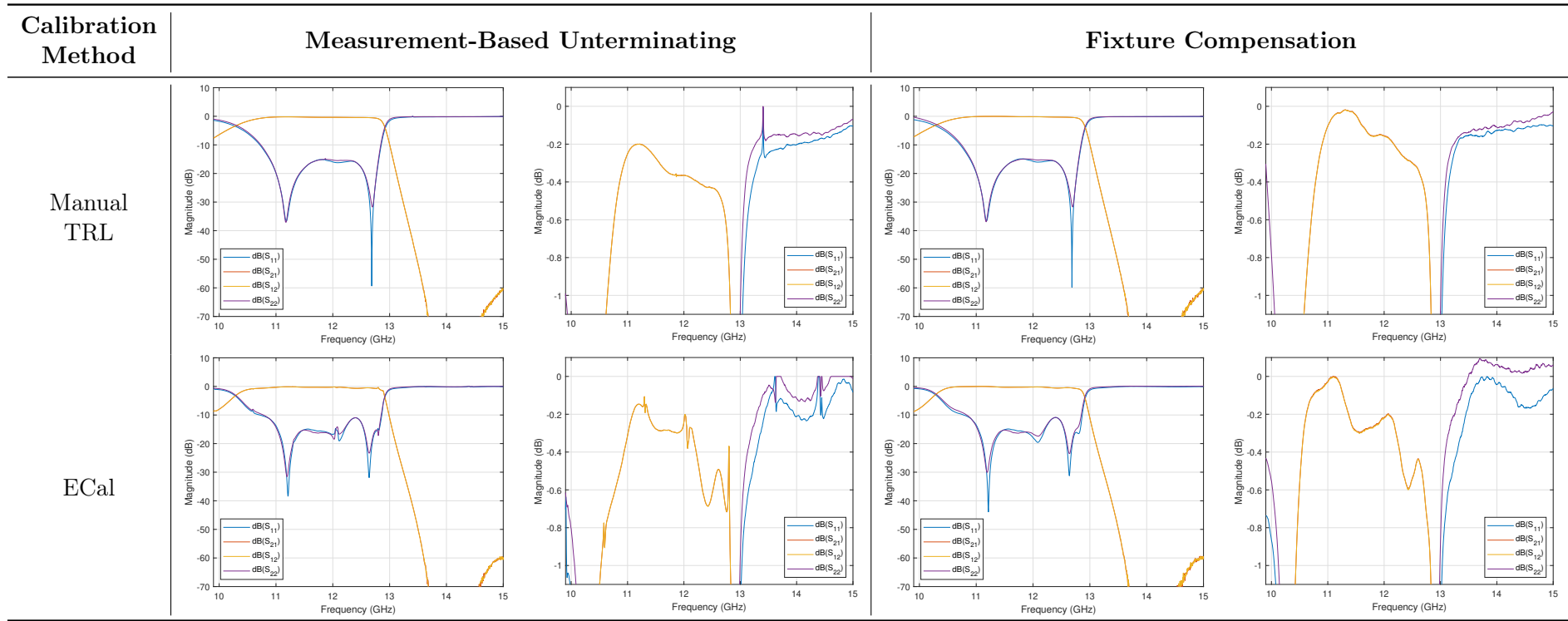


Figure B.1: MW13200 de-embedded S -parameters method comparison

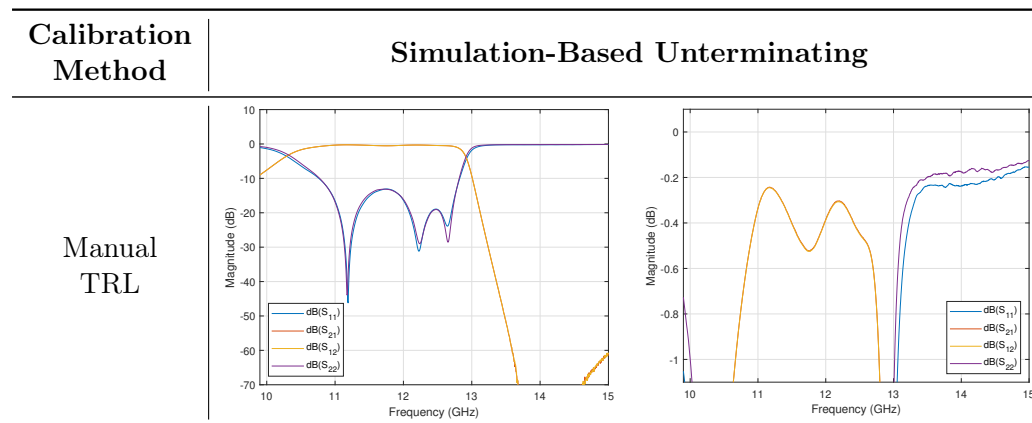


Figure B.2: MW13200 de-embedded S -parameters for simulation-based unterminating

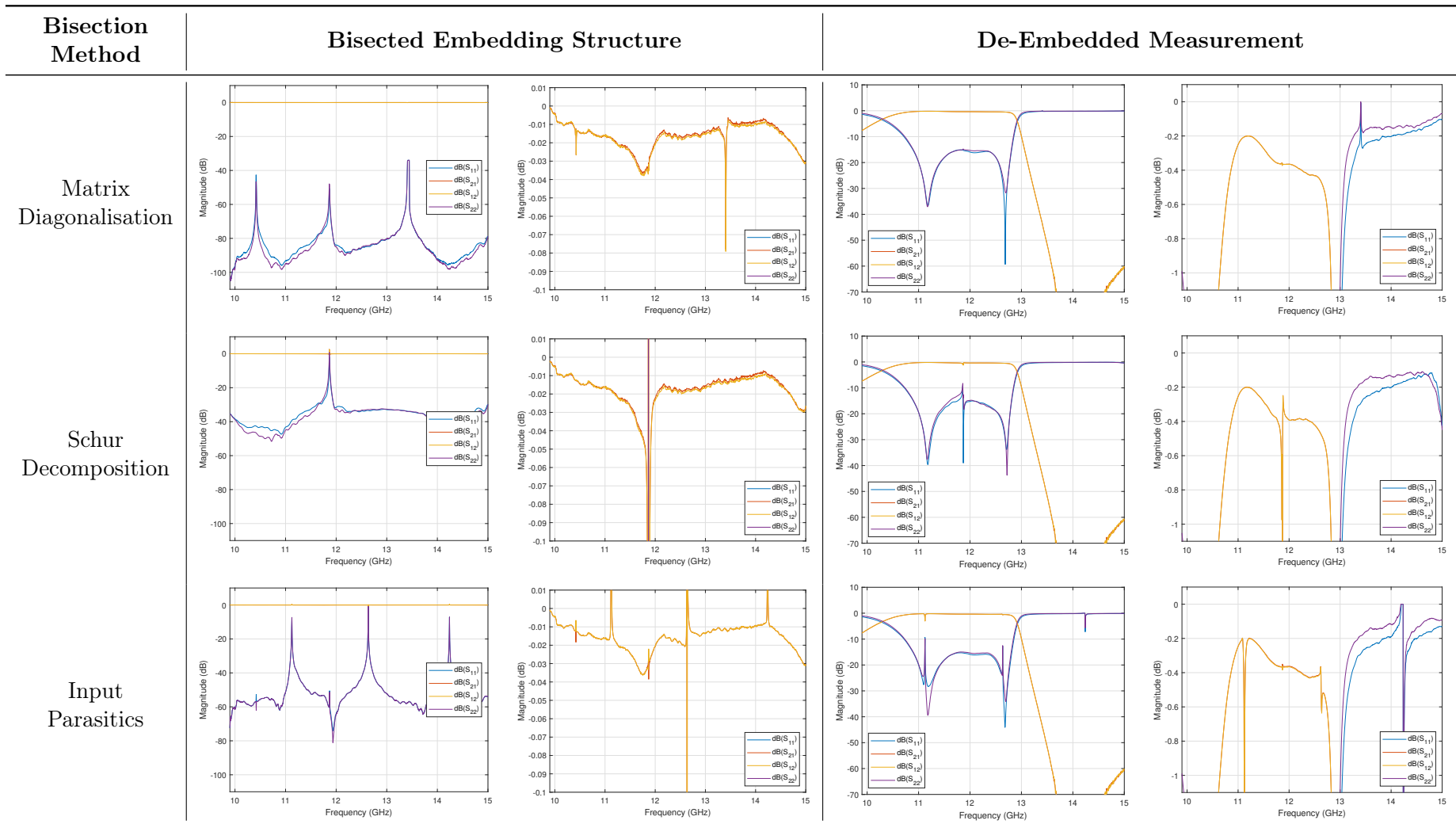


Figure B.3: MW13200 de-embedded S -parameters unterminating comparison

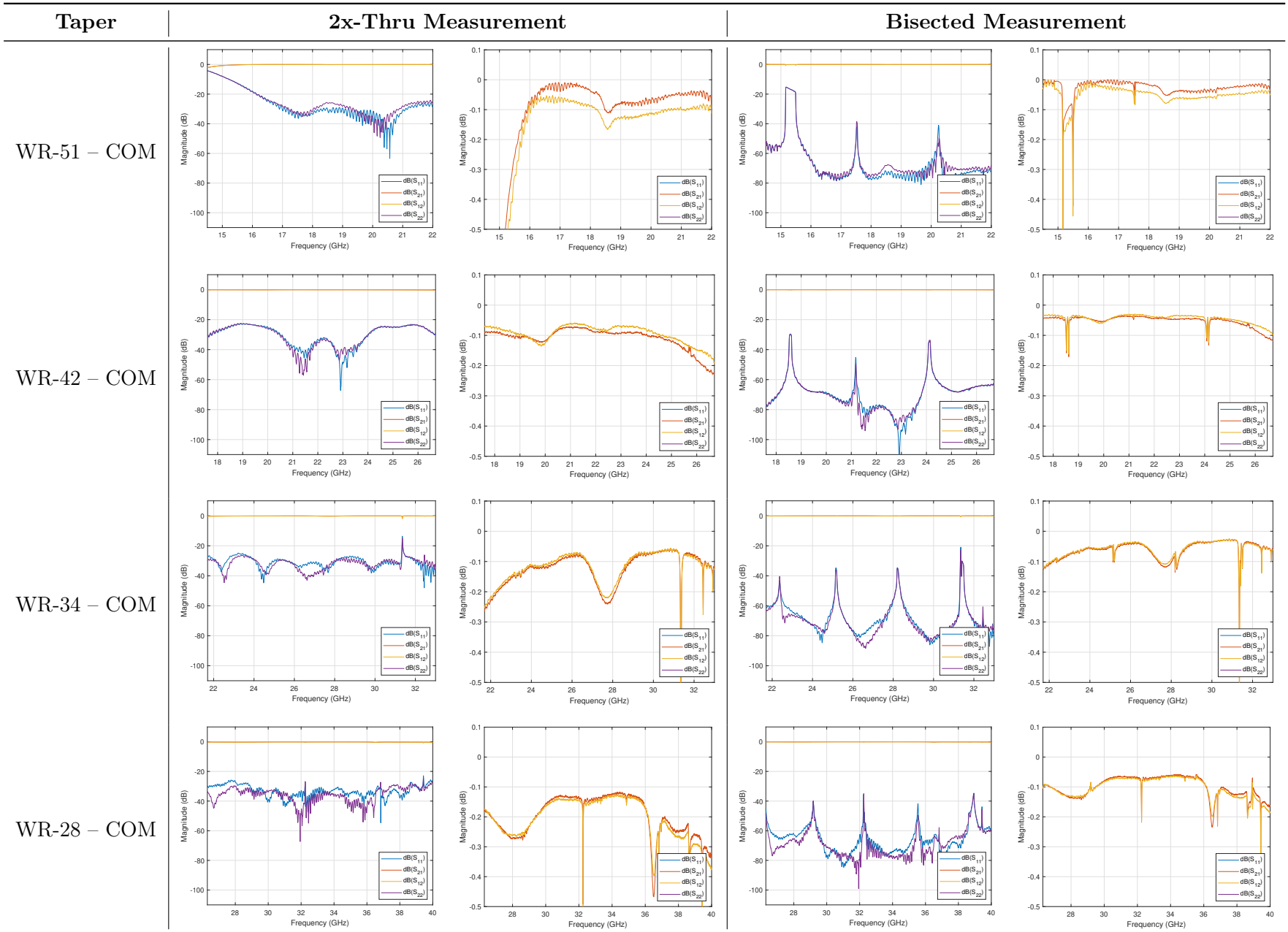


Figure B.4: 2x-thru and bisected measurements of COM tapers

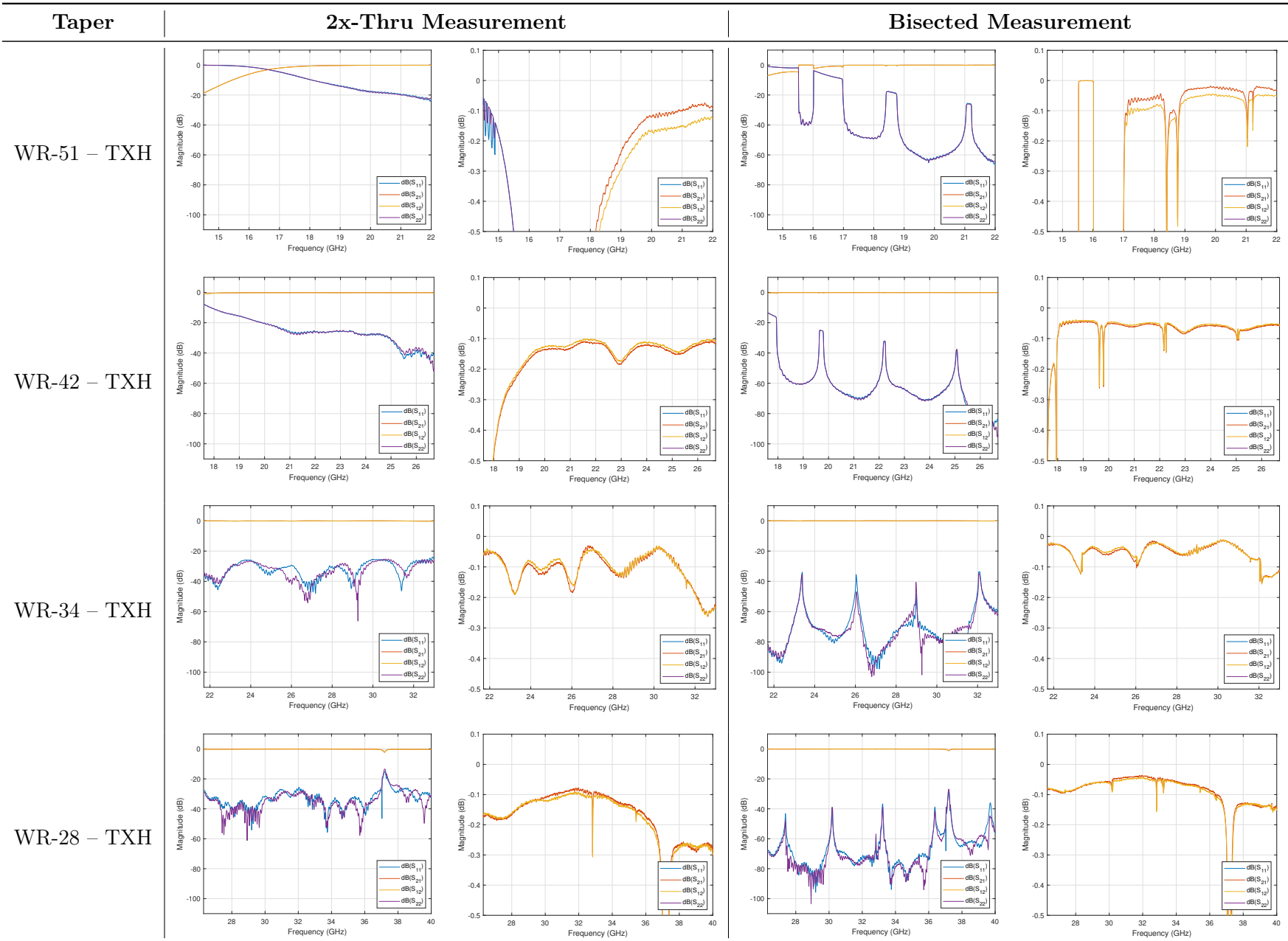


Figure B.5: 2x-thru and bisected measurements of TXH tapers

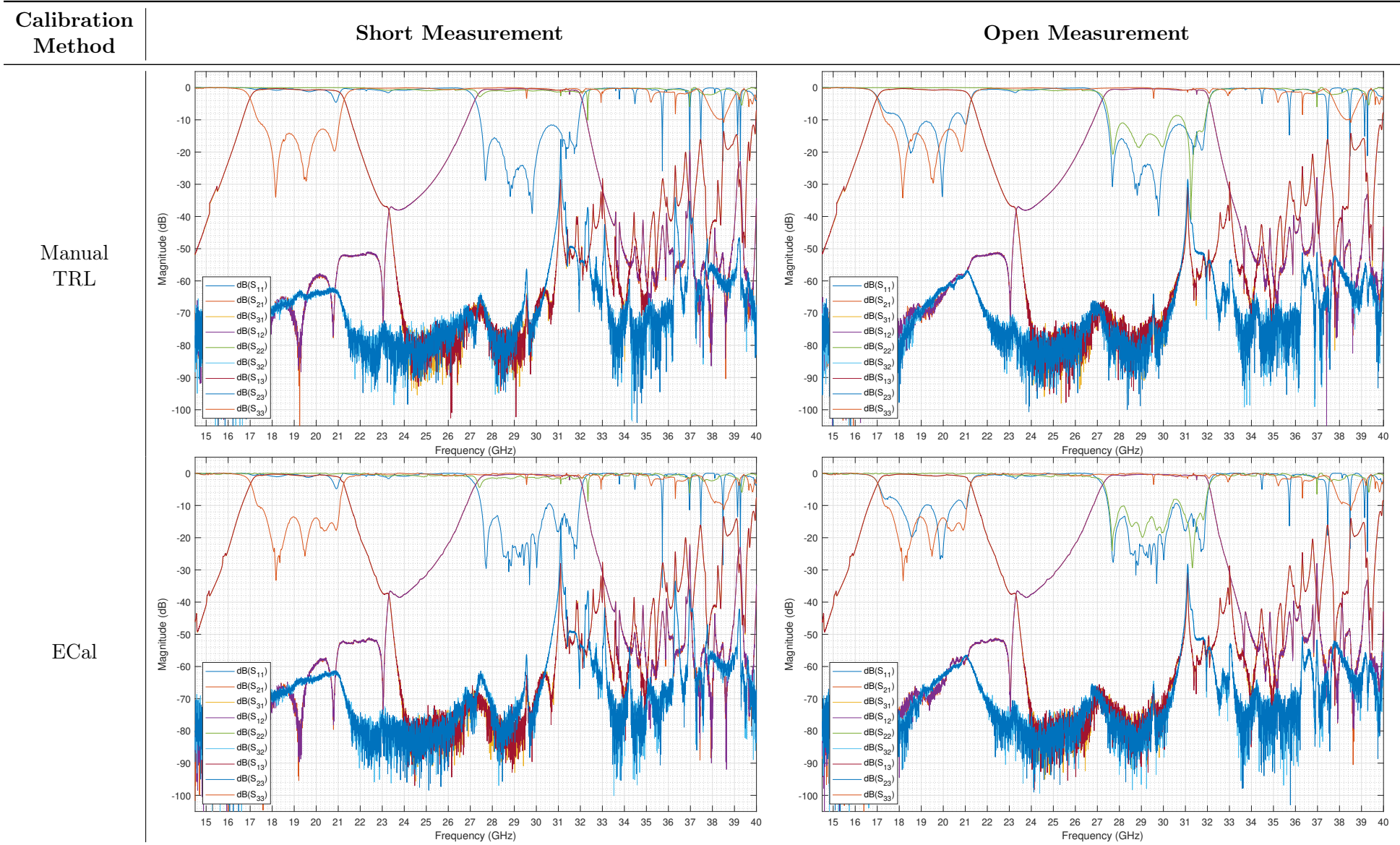


Figure B.6: Diplexer measurement method comparison

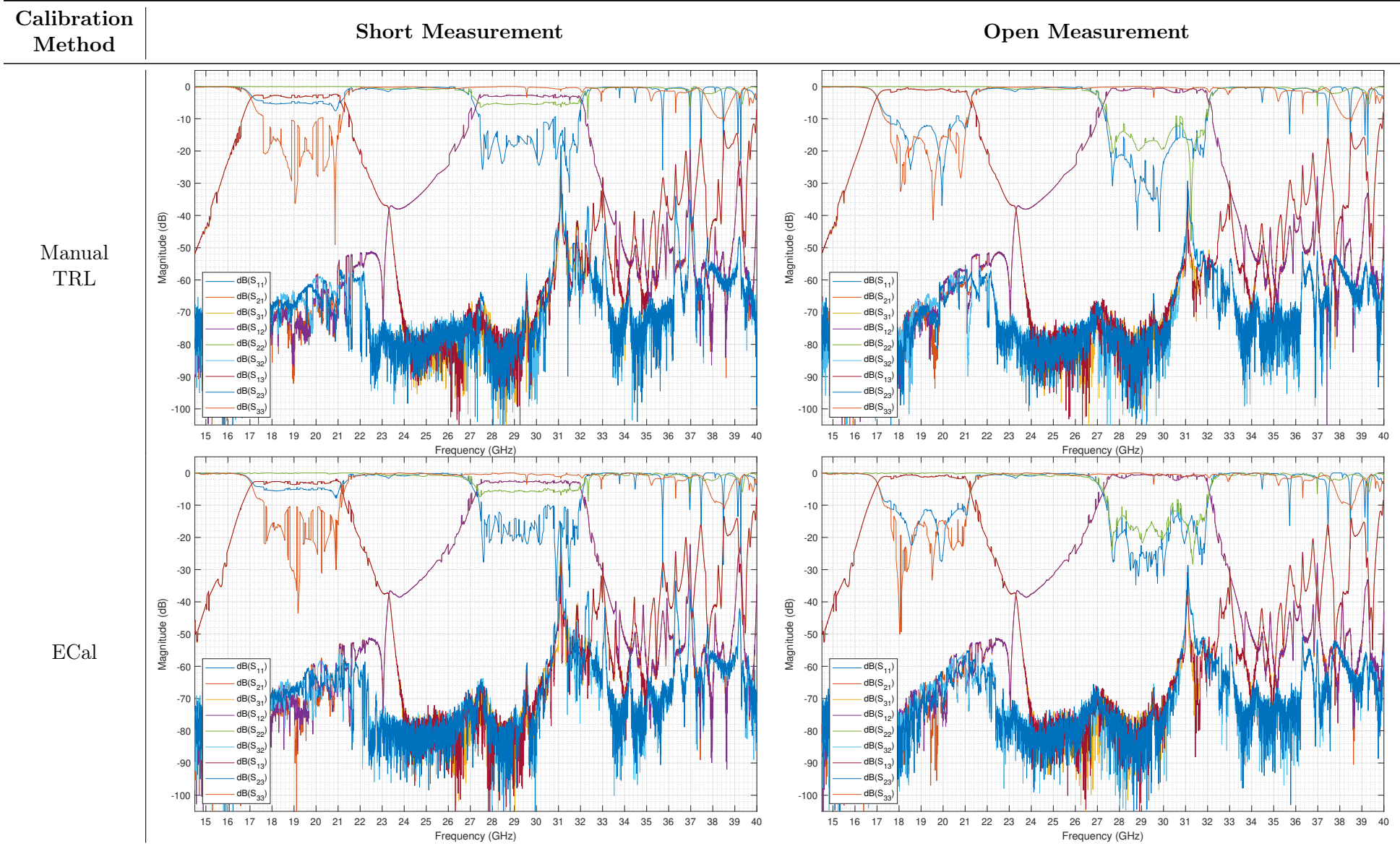


Figure B.7: Passivated diplexer measurement method comparison

C

Code Listings

C.1 Taper Design

Listing C.1: Johnson [4] MATLAB implementation

```
1 function [L, VSWR] = johnson(W0, W1, f, maxL)
2 %JOHNSON Provides a plot for ideal taper length based on Johnson (1959)
3
4 a0 = W0(1);
5 b0 = W0(2);
6 a1 = W1(1);
7 b1 = W1(2);
8
9 c = 3e8;
10
11 for i = 1:length(f)
12
13     lambda = c./f(i);
14
15     L = (0:0.1:maxL) * 1e-3;
16     l = 1./lambda .* sqrt(1-(lambda./(2*a1)).^2) .* L';
17
18     K0 = ( (b1-b0)./b0 - (a1-a0)./a0 ) / ( 1-(lambda/(2*a0))^2 ) ...
19         / ( (1-(lambda/(2*a0))^2)^(1/2) );
20     K1 = ( (b1-b0)./b1 - (a1-a0)./a1 ) / ( 1-(lambda/(2*a1))^2 ) ...
21         / ( (1-(lambda/(2*a1))^2)^(1/2) );
22
23     refl = 1./(L'./lambda) .* ( (K0.^2+K1.^2)/(64*pi^2) ...
24         - ((K0.*K1)/(32*pi^2)).*cos(4*pi*l) ).^(1/2);
25
26     refl_max = min(1, refl);
27
28     if not(isreal(refl_max))
29         refl_max(1:end) = nan;
30     end
31
32     VSWR(i,:) = (1+refl_max)./(1-refl_max);
33
34 end
35
36 end
```

C.2 Unterminating

Listing C.2: 2x-thru measurement bisection MATLAB implementation

```

1 function [A_in] = bisect(input,method)
2 %BISECT Bisects 2x-thru measurements according to different methods
3
4 Sobj_thru = makepassive(sparameters(strcat(input, '.s2p')));
5 S_thru = Sobj_thru.Parameters;
6 freq = Sobj_thru.Frequencies;
7
8 A_thru = s2abcd(S_thru);
9 Z_thru = s2z(S_thru);
10 Z_x = 1j* imag(Z_thru);
11 A_x = z2abcd(Z_x);
12
13 % Three methods of determining A_in
14 A_in_diag = zeros(2,2,length(freq));
15 A_in_simion = zeros(2,2,length(freq));
16 A_in_sqrtm = zeros(2,2,length(freq));
17
18 for i = 1:length(S_thru)
19     [P_diag,D_diag] = eig(A_thru(:,:,i));
20     [P_simion,D_simion] = eig(A_x(:,:,i));
21
22     A_in_diag(:,:,i) = P_diag * sqrtm(abs(real(D_diag)) ...
23         + 1j*abs(imag(D_diag))) * P_diag^-1;
24     A_in_simion(:,:,i) = sqrtm(inv(A_x(:,:,i))) ...
25         * sqrtm( sqrtm(A_x(:,:,i)) * A_thru(:,:,i) * sqrtm(A_x(:,:,i)) ) ...
26         * sqrtm(inv(A_x(:,:,i))));
27     A_in_sqrtm(:,:,i) = sqrtm(A_thru(:,:,i));
28 end
29
30 switch method
31     case 'diag'
32         A_in = A_in_diag;
33     case 'simion'
34         A_in = A_in_simion;
35     case 'sqrtm'
36         A_in = A_in_sqrtm;
37     otherwise
38         error(Invalid method: 'diag'/'simion'/'sqrtm')
39 end
40
41 end

```

C.3 De-Embedding

Listing C.3: *ABCD* de-embedding MATLAB implementation

```

1 function A_DUT = deembed(A_left,A_casc,A_right)
2 %DEEMBED Deembeds the left and right fixtures of an ABCD parameter cascade
3
4 A_DUT = zeros(2,2,length(A_casc));
5 for i = 1:length(A_casc)
6     A_DUT(:,:,i) = inv(A_left(:,:,i)) * A_casc(:,:,i) * inv(A_right(:,:,i));
7 end
8
9 end

```

C.4 Port Augmentation

Listing C.4: Rolfes and Schiek [44] MATLAB implementation

```

1 close all
2 clear
3 clc
4
5 %% Parameter Definition
6
7 % Ports
8 % 1 – COM
9 % 2 – TXH
10 % 3 – RXL
11
12 % Define file parameters
13 folder = 'diplexer\';
14 WG = 'WR28';
15 cal = 'Ecal';
16 version = '-short.s2p';
17
18 % Define reflection coefficient
19 refl_coeff = 0;
20
21 Sobj_21 = sparameters(strcat(folder,WG,'-H-COM-',cal,version));
22 Sobj_31 = sparameters(strcat(folder,WG,'-L-COM-',cal,version));
23 Sobj_23 = sparameters(strcat(folder,WG,'-H-L-',cal,version));
24
25 % Permute port order
26 Sobj_12 = smp2snp(Sobj_21,[2 1]);
27 Sobj_13 = smp2snp(Sobj_31,[2 1]);
28 % Sobj_23 = smp2snp(Sobj_23,[2,1]);
29
30 freq = Sobj_21.Frequencies;
31 refl = repmat(diag(repmat(refl_coeff,[3,1])),1,1,length(freq));
32
33 %% De-Embedding
34
35 A_12 = s2abcd(Sobj_12.Parameters);

```

```

36 A_13 = s2abcd(Sobj_13.Parameters);
37 A_23 = s2abcd(Sobj_23.Parameters);
38
39 A_COM = bisect(strcat(folder,WG,'-COM-',cal),'diag');
40 A_TXH = bisect(strcat(folder,WG,'-TXH-',cal),'diag');
41
42 S_dem_12 = abcd2s(deembed(A_COM,A_12,A_TXH));
43 S_dem_13 = abcd2s(deembed(A_COM,A_13,A_COM));
44 S_dem_23 = abcd2s(deembed(A_TXH,A_23,A_COM));
45
46 %% Taper Plotting
47
48 switch WG
49     case 'WR51'
50         xplotlim = [14.5,22.0];
51     case 'WR42'
52         xplotlim = [17.6,26.7];
53     case 'WR34'
54         xplotlim = [21.7,33.0];
55     case 'WR28'
56         xplotlim = [26.3,40.0];
57 end
58
59 %% Parameter Allocation
60
61 a = repmat([0,0,1;1,0,0;0,1,0],1,1,length(freq));
62 at = repmat([0,1,0;0,0,1;1,0,0],1,1,length(freq));
63
64 m = [zeros(1,1,length(freq)) S_dem_13(1,2,:)      S_dem_12(1,1,:)      ; ...
65      S_dem_23(1,1,:)      zeros(1,1,length(freq)) S_dem_12(2,1,:)      ; ...
66      S_dem_23(2,1,:)      S_dem_13(2,2,:)      zeros(1,1,length(freq)) ];
67
68 mt = [zeros(1,1,length(freq)) S_dem_13(1,1,:)      S_dem_12(1,2,:)      ; ...
69       S_dem_23(1,2,:)      zeros(1,1,length(freq)) S_dem_12(2,2,:)      ; ...
70       S_dem_23(2,2,:)      S_dem_13(2,1,:)      zeros(1,1,length(freq)) ];
71
72 G = a - pagetimes(refl,m);
73 Gt = at - pagetimes(refl,mt);
74
75 %% Wave Identification
76
77 b = zeros(3,3,length(freq));
78
79 for i = 1:length(freq)
80
81     b(1,1,i) = ...
82         ( G(3,1,i) * ( G(2,3,i) * ( a(1,2,i)*mt(1,3,i) - at(1,3,i)*m(1,2,i) ) ...
83         + Gt(2,3,i) * ( a(1,3,i)*m(1,2,i) - a(1,2,i)*m(1,3,i) ) ) ...
84         + G(2,1,i)*G(3,2,i) * ( a(1,3,i)*mt(1,3,i) - at(1,3,i)*m(1,3,i) ) ) ...
85         / ( G(3,2,i) * ( G(1,3,i)*Gt(2,3,i) - Gt(1,3,i)*G(2,3,i) ) );
86
87     b(2,2,i) = ...
88         ( G(1,2,i) * ( G(3,1,i) * ( a(2,3,i)*mt(2,1,i) - at(2,1,i)*m(2,3,i) ) ...
89         + Gt(3,1,i) * ( a(2,1,i)*m(2,3,i) - a(2,3,i)*m(2,1,i) ) ) ...
90         + G(1,3,i)*G(3,2,i) * ( a(2,1,i)*mt(2,1,i) - at(2,1,i)*m(2,1,i) ) ) ...

```

```

91         /( G(1,3,i) * (G(2,1,i)*Gt(3,1,i) - Gt(2,1,i)*G(3,1,i)) );
92
93     b(3,3,i) = ...
94         ( G(2,3,i) * ( G(1,2,i) * (at(3,2,i)*m(3,1,i) - a(3,1,i)*mt(3,2,i)) ...
95         + Gt(1,2,i) * (a(3,1,i)*m(3,2,i) - a(3,2,i)*m(3,1,i)) ) ...
96         + G(2,1,i)*G(1,3,i) * (at(3,2,i)*m(3,2,i) - a(3,2,i)*mt(3,2,i)) ) ...
97         /( G(2,1,i) * (G(1,2,i)*Gt(3,2,i) - Gt(1,2,i)*G(3,2,i)) );
98
99 end
100
101 %% Matrix Computation
102
103 S = pagemrdivide((b+m),(pagemtimes(refl,b) + a));
104
105 SDUT = sparameters(S,freq,50);
106 rfplot(SDUT)

```

C.5 Data Fusion

Listing C.5: Waveguide data fusion MATLAB implementation

```

1 close all
2 clear
3 clc
4
5 % Define method to be used and file name
6
7 method = 'TRL-open';
8 name = 'file1'
9
10 %% Data Loading
11
12 obj51 = sparameters(strcat('diplexer/merged-WR51',method,'.s2p'));
13 obj42 = sparameters(strcat('diplexer/merged-WR42',method,'.s2p'));
14 obj34 = sparameters(strcat('diplexer/merged-WR34',method,'.s2p'));
15 obj28 = sparameters(strcat('diplexer/merged-WR28',method,'.s2p'));
16
17 f51 = [obj51.Frequencies(1) obj51.Frequencies(end)];
18 f42 = [obj42.Frequencies(1) obj42.Frequencies(end)];
19 f34 = [obj34.Frequencies(1) obj34.Frequencies(end)];
20 f28 = [obj28.Frequencies(1) obj28.Frequencies(end)];
21
22 % Define indicies of overlapping frequency segments
23
24 f51i = [ ...
25     find(obj51.Frequencies == f51(1)) ...
26     find(obj51.Frequencies == f42(1)) ...
27     find(obj51.Frequencies == f34(1)) ...
28     find(obj51.Frequencies == f51(2))];
29
30 f42i = [ ...
31     find(obj42.Frequencies == f42(1)) ...
32     find(obj42.Frequencies == f34(1)) ...

```

```

33     find(obj42.Frequencies == f51(2)) ...
34     find(obj42.Frequencies == f28(1)) ...
35     find(obj42.Frequencies == f42(2))];
36
37 f34i = [ ...
38     find(obj34.Frequencies == f34(1)) ...
39     find(obj34.Frequencies == f51(2)) ...
40     find(obj34.Frequencies == f28(1)) ...
41     find(obj34.Frequencies == f42(2)) ...
42     find(obj34.Frequencies == f34(2))];
43
44 f28i = [ ...
45     find(obj28.Frequencies == f28(1)) ...
46     find(obj28.Frequencies == f42(2)) ...
47     find(obj28.Frequencies == f34(2)) ...
48     find(obj28.Frequencies == f28(2))];
49
50 step = 5e6;
51
52 %% Data fusion across frequency segments
53
54 freq_t = (obj51.Frequencies(1):step:obj28.Frequencies(end))';
55
56 Stot = cat(3, ...
57     obj51.Parameters(:, :, f51i(1):f51i(2)), ...
58     power( obj51.Parameters(:, :, f51i(2)+1:f51i(3)) .* ...
59         obj42.Parameters(:, :, f42i(1)+1:f42i(2)) , 1/2 ), ...
60     power( obj51.Parameters(:, :, f51i(3)+1:f51i(4)) .* ...
61         obj42.Parameters(:, :, f42i(2)+1:f42i(3)) .* ...
62         obj34.Parameters(:, :, f34i(1)+1:f34i(2)) , 1/3 ), ...
63     power( obj42.Parameters(:, :, f42i(3)+1:f42i(4)) .* ...
64         obj34.Parameters(:, :, f34i(2)+1:f34i(3)) , 1/2 ), ...
65     power( obj42.Parameters(:, :, f42i(4)+1:f42i(5)) .* ...
66         obj34.Parameters(:, :, f34i(3)+1:f34i(4)) .* ...
67         obj28.Parameters(:, :, f28i(1)+1:f28i(2)) , 1/3 ), ...
68     power( obj34.Parameters(:, :, f34i(4)+1:f34i(5)) .* ...
69         obj28.Parameters(:, :, f28i(2)+1:f28i(3)) , 1/2 ), ...
70     obj28.Parameters(:, :, f28i(3)+1:f28i(4)));
71
72 Sobj = (sparameters(Stot, freq_t));
73 Sobj.Parameters(abs(Sobj.Parameters)>=1) = 1;
74
75 %% Plotting
76
77 figure('Position', [100, 100, 1000, 600])
78 rfplot(Sobj)
79 legend('Location', 'southwest')
80 grid minor
81 % xlim([14.5, 40])
82 % xlim([16, 21])
83 % ylim([-105, 5])
84 % ylim([-1.1, 0.1])
85 % xticks([15:1:40])

```